A Conceptual Performance Study on a Two-Look ScanSAR Mode Configuration for the Forthcoming ROSE-L Mission

Stefano Perna, *Senior Member, IEEE*, Francesco Longo, Simona Zoffoli, Malcolm Davidson, Lorenzo Iannini, and Riccardo Lanari, *Fellow, IEEE*

The authors would like to dedicate this article to the memory of their colleague and friend Mariarosaria Manzo, wife of the first author. Her intelligence, passion, courage, and poise along with her contributions in the field of SAR interferometry are the legacy that has inspired this work.

***Abstract*— This work shows that additional ScanSAR capabilities, with respect to those achievable through the current synthetic aperture radar (SAR) system of the forthcoming Radar Observation System for Europe at L-band (ROSE-L) mission, may be easily enabled through a proper shaping of the azimuth pattern of the TX radar antenna. In particular, we show that by properly acting only on the distribution of the input excitations of the elements of the currently designed TX antenna array, we can move from a single azimuth-look ScanSAR configuration to a more attractive two-look one. This result is achieved without upsetting the current system architecture and without changing the current mission parameters [such as azimuth resolution, range swath, and pulse repetition frequency (PRF)], all tailored to a one-look ScanSAR configuration. On the other hand, the proposed two-look mode requires to double the azimuth beamwidth with respect to the one-look mode, thus leading to an unavoidable antenna gain decrease, whose amount is approximately 3 dB. The presented analysis also shows that, by still acting on the distribution of the input excitations of the TX antenna array, the scalloping effect can be significantly mitigated with respect to that of the current system design, in both scenarios relevant to the original one-look ScanSAR configuration and the proposed two-look one.**

***Index Terms*— Array synthesis, scalloping mitigation, ScanSAR, synthetic aperture radar (SAR), two-look ScanSAR.**

Manuscript received 18 July 2022; revised 14 January 2023, 21 June 2023, and 9 September 2023; accepted 5 December 2023. Date of publication 18 December 2023; date of current version 8 January 2024. This work was supported in part by the Italian Space Agency through the Agreement n. 2022-6-HH.0 "SAR-L: consolidamento della scienza". *(Corresponding author: Riccardo Lanari.)*

Stefano Perna is with the Department of Engineering (DI), Università degli Studi di Napoli "Parthenope," 80143 Naples, Italy, and also with the Institute for Remote Sensing of the Environment (IREA), Italian National Research Council (CNR), 80124 Naples, Italy (e-mail: stefano.perna@uniparthenope.it).

Francesco Longo and Simona Zoffoli are with the Italian Space Agency (ASI), 80133 Rome, Italy (e-mail: francesco.longo@asi.it; simona.zoffoli@asi.it).

Malcolm Davidson is with the Earth and Mission Science Division, European Space Research and Technology Centre (ESTEC), European Space Agency (ESA), 2201 Noordwijk, The Netherlands (e-mail: malcolm.davidson@esa.int).

Lorenzo Iannini is with Aurora Technology for ESA - European Space Agency, European Space Research and Technology Centre (ESA-ESTEC), 2201 Noordwijk, The Netherlands (e-mail: lorenzo.iannini@esa.int).

Riccardo Lanari is with the Institute for Remote Sensing of the Environment (IREA), Italian National Research Council (CNR), 80124 Naples, Italy (e-mail: lanari.r@irea.cnr.it).

Digital Object Identifier 10.1109/TGRS.2023.3344537

I. Introduction

THE forthcoming synthetic aperture radar (SAR) Radar Observation System for Europe at L-band (ROSE-L) mission [1], [2], supported by the European Space Agency (ESA), Paris, France, as part of the Copernicus Expansion Programme, will benefit from the synergic use of advanced acquisition modes and/or optimization strategies mainly aimed at achieving a high-resolution and wide-swath (HRWS) capability [3]. In particular, according to the current system design, the implemented ScanSAR acquisition mode [4] will be enhanced through the joint use of the scan on receive (SCORE) [5], [6] and the displaced phase center (DPC) [6], [7], [8] acquisition techniques.

To achieve these advanced capabilities, proper requirements have been considered during the design of the radar antenna of the ROSE-L system. Indeed, to implement the ScanSAR and SCORE techniques, reconfigurability of the antenna pattern along the elevation angle must be ensured. Moreover, to implement the DPC technique, the radar antenna consists of five panels (displaced in the along-track direction) that cooperate as a five-element linear array [9] in the TX mode, whereas they work separately in the RX one.

In this work, starting from the preliminary findings discussed in [10], we present the results of a conceptual performance study showing that we can easily move from a single azimuth-look ScanSAR configuration, to which the ROSE-L system has been originally designed, to a two-look one, with several advantages in different applications. In this regard, it is remarked the increasing interest of the scientific community toward the possible availability of a ROSE-L two-look mode configuration, see, for instance, the contribution in [11] relevant to the corresponding along-track surface deformation component retrieval capability.

We underline that it is well-known that SAR systems based on the burst mode technology [12] may allow to achieve, through the proper overlapping between the images relevant to adjacent bursts, more than one look. This was the case with the SRTM mission in 2000 (two looks were achieved in the far-range swaths [13] with the ScanSAR mode) and, subsequently, in 2002 with ENVISAT (where, as a matter of fact, a three-look ScanSAR mode is exploited by the advanced SAR (ASAR) sensor [14], [15]), just to mention some missions with this capability. More recently, some experiments [16], [17] have shown that a two-look configuration can be achieved also with the TerraSAR-X system, particularly with the ScanSAR

and Terrain Observation with Progressive Scans (TOPS) [18] burst modes, originally designed for a one-look configuration. In particular, in [16] and [17], it is shown that this advanced observation capability can be achieved with TerraSAR-X at the expenses of a degradation (of about a factor 2) of the azimuth resolution achievable with the originally designed one-look burst mode configurations.

In this work, we show that a two-look ScanSAR mode can be achieved also with the forthcoming ROSE-L system, originally designed for a one-look configuration, without modifying the original mission parameters (such as azimuth resolution and range swath, just to quote those directly related to the HRWS capability of the system) and with a negligible impact on the realization of the already designed radar antenna. In particular, we show how to take benefit from the availability of the five azimuth panels of the originally designed ROSE-L antenna array to properly shape the illuminated azimuth beam to enable additional ScanSAR capabilities with respect to those achievable through the original ROSE-L radar design. More specifically, we show that by properly acting only on the distribution of the input excitations of the five array panels, we can easily achieve a two-look ScanSAR mode. Moreover, we also show that by still acting on the distribution of the input excitations of the TX array panels, the scalloping effect [12] can be significantly mitigated with respect to that of the original system design, in both scenarios relevant to the original one-look ScanSAR configuration and the proposed two-look one.

To calculate the array input excitations enabling the above-mentioned improvements of the ROSE-L ScanSAR mode capabilities, we have implemented an array synthesis algorithm based on a global optimization procedure, which takes benefit from the very reduced number of unknowns involved in the problem at hand. A number of figures of merit have been introduced to evaluate the performance of the synthesized arrays and to highlight the achieved improvements.

It is remarked that this work is aimed neither at presenting a novel SAR acquisition mode nor at proposing a novel array synthesis algorithm. This article is indeed targeted at focusing on the forthcoming ROSE-L system and at showing how, with a negligible impact on the hardware design, it is possible to double the number of azimuth looks without impairing key mission parameters, specifically, the azimuth resolution and the range swath. In particular, to achieve the two-look ScanSAR mode configuration, which enriches the observation capabilities of the originally designed ROSE-L SAR system, we properly shape the radiated azimuth beam through an easy solution taking benefit from the well-known properties of the array antennas. We remark that the simplicity of the proposed solution, relevant to such a sophisticated and highly innovative radar sensor characterized by unprecedented engineering solutions, is a key point of this work.

In any case, the results of the presented analysis, although tailored to the ROSE-L SAR sensor, can be easily extended to other systems, thus representing a valuable instrument for the design of future missions.

This work is organized as follows. Section II describes the two-look ScanSAR mode that we propose to enable. Section III summarizes the main aspects of the current ROSE-L system design related to the analysis proposed in this work. In Section IV, some preliminary considerations for the achievement of the two-look ScanSAR mode with the ROSE-L system are addressed; moreover, some figures of merit adopted to discuss the results obtained in the work are introduced. In Sections V and VI, we describe the array synthesis algorithms that we implemented to achieve the proposed two-look ScanSAR mode and present the corresponding achieved results. Section VII includes a final discussion based on the results obtained in the previous sections. Section VIII reports the conclusion and final remarks.

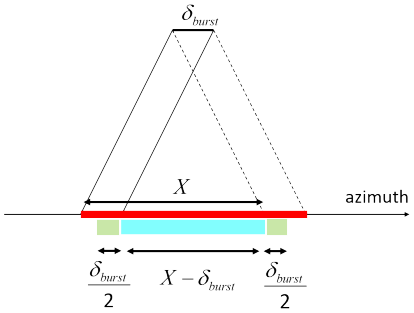

Fig. 1. Acquisition geometry relevant to a generic burst in the ScanSAR acquisition mode.

II. One-Look and Two-Look ScanSAR Modes

In this section, we introduce a ScanSAR configuration that we name two-look ScanSAR mode. To do this, let us consider the following quantities:

1) v: sensor velocity (or, more precisely, sensor-target velocity);
2) τ_{burst}: burst time duration;
3) T_{burst}: burst time period;
4) $\delta_{\text{burst}} = v\tau_{\text{burst}}$: space length associated with the burst time duration;
5) $\Delta_{\text{burst}} = v\text{T}_{\text{burst}}$: space period associated with the burst time period;
6) X: antenna azimuth footprint associated with the azimuth main beam

and refer to Fig. 1, where it is shown the ScanSAR acquisition geometry [12] relevant to a generic burst.

In Fig. 1, the area highlighted in red, whose length is equal to $X + \delta_{\text{burst}}$, collects all the targets illuminated by the antenna with its main beam while it acquires a generic burst. Note that not all the targets belonging to the red area can be focused with the same azimuth resolution. Moreover, in Fig. 1, among the targets of the red area, we have highlighted in cyan those illuminated by the antenna main beam during the overall burst duration τ_{burst}. As a matter of fact, the targets belonging to the cyan area of Fig. 1, whose extension is equal to $X - \delta_{\text{burst}}$, can be focused with the finest azimuth resolution, namely,

$$\Delta x_{\text{full}} = \frac{\lambda r}{2\delta_{\text{burst}}} \tag{1}$$

wherein r is the range coordinate and λ is the carrier wavelength. In Fig. 1, the two areas highlighted in green collect the targets illuminated by the antenna main beam for a time interval between $\tau_{\text{burst}}/2$ and τ_{burst}. For these targets, the degradation of the azimuth resolution is, therefore, smaller

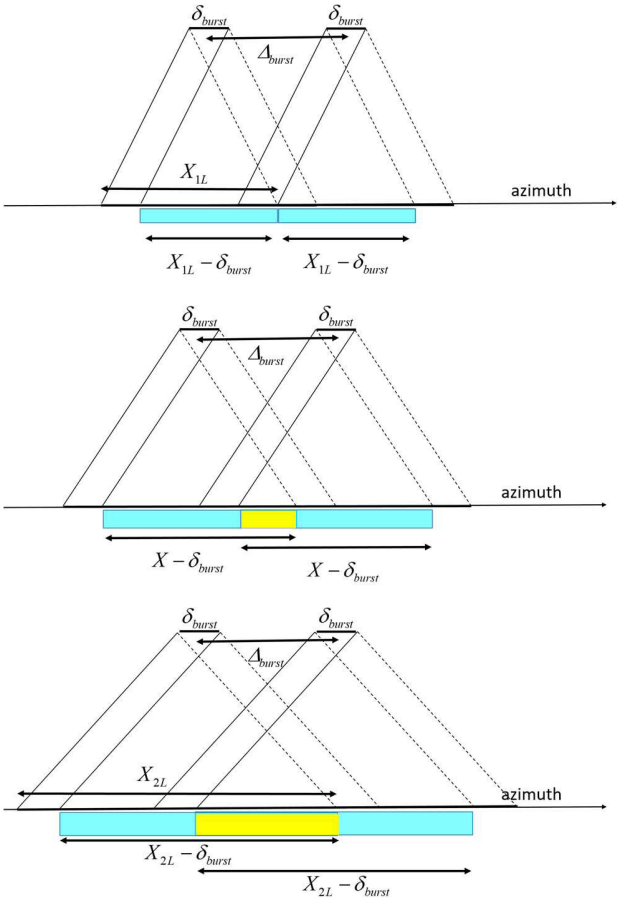

Fig. 2. One-look versus two-look ScanSAR modes. (top) One-look ScanSAR mode. (central) Between one-look and two-look ScanSAR modes. (bottom) Two-look ScanSAR mode.

than a factor 2 with respect to the finest one in (1). The length of each of these two green areas is equal to $\delta_{\text{burst}}/2$.

Let us now refer to Fig. 2 (top), where two adjacent bursts (that is, subsequent bursts relevant to the same range subswath) are depicted. When the cyan regions relevant to these two bursts touch each other without overlapping, no azimuth gaps will appear in the full-resolution SAR image relevant to the considered range subswath. In the following, we refer to this acquisition condition as the one-look acquisition ScanSAR mode. Indeed, after the burst mosaicking, one look at the finest azimuth resolution is available for all the targets belonging to the considered range subswath. To obtain such a one-look acquisition mode, the following condition must be enforced:

$$X = X_{1L} = \Delta_{\text{burst}} + \delta_{\text{burst}}. \tag{2}$$

When the antenna azimuth footprint X is smaller than the quantity X_{1L} in (2), then the cyan regions relevant to two adjacent bursts do not touch each other. This leads, after the burst mosaicking, to the presence of azimuth gaps in the full-resolution SAR image relevant to the considered range subswath. On the other side, when the antenna azimuth footprint X is larger than the quantity X_{1L} in (2), then the cyan regions relevant to the two considered bursts present an overlapping area, highlighted in yellow in the middle of Fig. 2.

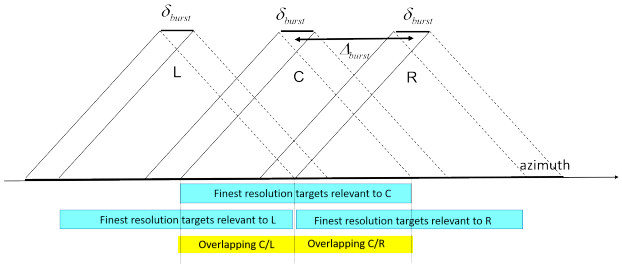

Fig. 3. Relevant to the two-look ScanSAR mode.

For the targets belonging to this overlapping (yellow) area, two different looks (one for each burst) are available with the finest resolution in (1). Of course, the larger the length of the azimuth footprint X, the wider the overlapping region highlighted in yellow in Fig. 2. One interesting case, still depicted in Fig. 2 (bottom), is represented by the following condition:

$$X = X_{2L} = 2\Delta_{\text{burst}} + \delta_{\text{burst}} \tag{3}$$

that guarantees the 50% overlapping between the cyan regions relevant to two adjacent bursts. Indeed, as shown in Fig. 3, when the condition in (3) is enforced, if we consider a generic burst, say central burst, it shares 100% of its finest resolution cyan area with the cyan areas associated with the two adjacent bursts, say left and right bursts. Therefore, the condition in (3) guarantees that for all the targets belonging to the considered range subswath, two different looks relevant to two opposite aspect angles (related to two adjacent bursts) are available with the finest resolution in (3). In the following, we refer to this acquisition condition as the two-look acquisition ScanSAR mode. This mode was exploited, for instance, during the SRTM mission for the far-range swaths [13] and subsequently with ENVISAT (where, as a matter of fact, a three-look ScanSAR mode is exploited [14], [15]).

More recently, a two-look configuration has been achieved also with the ScanSAR [17] and TOPS [16] modes of the TerraSAR-X system, originally designed for a one-look configuration; this advanced capability has been, however, achieved at the expenses of a degradation (of about a factor 2) of the azimuth resolution of the original one-look burst mode configurations. In this regard, it is remarked then if we pass from condition (2) to condition (3) by retaining the same values of Δ_{burst} and δ_{burst}, thus acting only on the azimuth beamwidth of the two-way antenna pattern, we do not modify the azimuth resolution of the system, see (1). For instance, for the three ScanSAR configurations depicted in Fig. 2, where the parameters Δ_{burst} and δ_{burst} do not change in the three panels, the azimuth resolution of the system is always the same. Summing up, as shown in Fig. 2, halfway between the one-look and two-look ScanSAR modes defined by the azimuth footprints X_{1L} in (2) and X_{2L} in (3), respectively, intermediate configurations characterized by an azimuth footprint $X \in [X_{1L}, X_{2L}]$ may be considered. In general, we can define the following index, say TLCP, which stands for

two-look coverage percentage:

$$\text{TLCP} = \frac{X - \Delta_{\text{burst}} - \delta_{\text{burst}}}{\Delta_{\text{burst}}}. \tag{4}$$

When $X \in [X_{1L}, X_{2L}]$, the TLCP in (4) ranges between 0 (when $X = X_{1L}$) and 1 (when $X = X_{2L}$), and represents, for a given range subswath, the (normalized) percentage of illuminated areas for which two different finest-resolution looks, relevant to two adjacent bursts, are available.

It is finally remarked that the condition in (2) can be relaxed as follows:

$$X = \tilde{X}_{1L} = \Delta_{\text{burst}} \tag{5}$$

if one accepts to exploit also the subresolution areas highlighted in green in Fig. 1, where the degradation of the azimuth resolution is smaller than a factor 2 with respect to the finest one in (1), to reconstruct the final SAR image through burst mosaicking. Similarly, the condition in (3) can be relaxed as follows:

$$X = \tilde{X}_{2L} = 2\Delta_{\text{burst}} \tag{6}$$

if one accepts once again to exploit also the subresolution areas highlighted in green in Fig. 1 to obtain for each target of a generic range subswath two different looks coming from two different bursts. Finally, the TLCP in (4) can be relaxed as follows:

$$\widetilde{\text{TLCP}} = \frac{X - \Delta_{\text{burst}}}{\Delta_{\text{burst}}} = \text{TLCP} + \xi \tag{7}$$

where

$$\xi = \frac{\delta_{\text{burst}}}{\Delta_{\text{burst}}} \approx \frac{1}{N_B} \tag{8}$$

being N_B the number of range subswaths used by the ScanSAR system to cover the entire range swath. When $X \in [\tilde{X}_{1L}, \tilde{X}_{2L}]$, the $\widetilde{\text{TLCP}}$ in (7) ranges between 0 (when $X = \tilde{X}_{1L}$) and 1 (when $X = \tilde{X}_{2L}$), and represents, for a given range subswath, the (normalized) percentage of illuminated areas for which two different looks with azimuth resolution $\Delta x \in [\Delta x_{\text{full}}, 2\Delta x_{\text{full}}]$ and relevant to two different bursts are available.

Summing up, in the subsequent analysis, we refer to the three following ScanSAR modes, all characterized by the same burst duration and period.

One-Look Mode. For this mode, the full-resolution regions relevant to two adjacent bursts touch each other (nearly) without overlapping. After the burst mosaicking, for all the targets belonging to the considered range subswath, one look at the finest azimuth resolution in (1) is always available. For this acquisition mode, the azimuth footprint is given in (2).

Full Two-Look Mode. For this mode, the full-resolution regions (namely, the areas where $\Delta x = \Delta x_{\text{full}}$) relevant to two adjacent bursts present a 50% overlapping. For all the targets belonging to the considered range subswath, two different looks, coming from two adjacent bursts, are always available with the finest resolution in (1). For this acquisition mode, the azimuth footprint is given in (3).

Bulk Two-Look Mode. For this mode, the almost-full resolution regions (namely, the areas where $\Delta x \in [\Delta x_{\text{full}}, 2\Delta x_{\text{full}}]$) relevant to two adjacent bursts present a 50% overlapping. For all the targets belonging to the considered range subswath, two different looks, coming from two adjacent bursts, are always available with resolution $\Delta x \in [\Delta x_{\text{full}}, 2\Delta x_{\text{full}}]$. For this acquisition mode, the azimuth footprint is given in (6).

It is remarked that different application scenarios could profitably take advantage from the availability of a two-look ScanSAR mode. For instance, the enlargement of the azimuth beamwidth involves an extension of the overall imaged Doppler spectrum component that, at least in principle, may be exploited to improve the azimuth resolution. Moreover, ASAR-focusing approaches, accounting for the available two-look burst raw data, can be exploited (see, for instance, [19]). Also, a two-look amplitude image multilooking can be carried out (even through optimized look weighting solutions, see [20]) at a global scale without impairment of the azimuth resolution of the generated images. Furthermore, a two-look complex multilooking can be carried out at a global scale without impairing the azimuth resolution of the generated SAR interferograms. On the other side, fast motions occurring in the observed area can be retrieved, without azimuth gaps, by exploiting the azimuthal temporal diversity between the overlapping images relevant to adjacent bursts. Moreover, the azimuthal angular diversity (i.e., different squint angles) between the overlapping images relevant to the adjacent bursts can be exploited in differential SAR interferometry (DInSAR) applications to retrieve, at the global scale and without azimuth gaps, the North–South deformation components of the displacement phenomena occurred on the ground [21]. By way of example, the last application scenario is analyzed in more detail in Appendix A.

III. ROSE-L Case Study: Current Design

We now summarize the main characteristics of the ROSE-L system that are useful for the analysis presented in this work. More details on the system performance can be found in [1].

A. System Description

According to the recent technological trends, the system is aimed at pursuing a wide swath capability while limiting the related azimuth resolution degradation. To do this, different advanced acquisition techniques, namely, ScanSAR [3], [4], [12], SCORE [5], [6], and DPC [6], [7], [8], will be simultaneously experienced.

More specifically, the ScanSAR mode [12] is implemented through the use of three range subswaths, partly overlapping each other. These three subswaths can be picked up from a set of four potential subswaths whose look angle ranges from about 25° to 47°. Among these four subswaths, in the following, we will focus on the three ones leading to a range swath similar to that of the Sentinel-1 sensors [22]. The parameters of the corresponding bursts are reported in Table I. In each subswath, the SCORE technique [5], [6] is implemented. Finally, to reduce the azimuth ambiguities while

TABLE I
MAIN CHARACTERISTICS OF THE ROSE-L SCANSAR BURSTS

Main characteristics of the ROSE-L ScanSAR bursts			
	Burst 1	**Burst 2**	**Burst 3**
Burst duration β [sec.]	1.18	1.25	1.33
Look angle [deg.]	31.3 – 37.2	37.0 – 42.3	42.1 – 46.8

TABLE II
ANTENNA AZIMUTH FOOTPRINT REQUIRED FOR DIFFERENT ROSE-L SCANSAR MODES

Antenna azimuth footprint required for the different ROSE-L ScanSAR modes			
	Burst 1 [Km]	**Burst 2** [Km]	**Burst 3** [Km]
One-look mode	35.568	36.072	36.648
Bulk two-look mode	54.144	54.144	54.144
Full two-look mode	62.640	63.144	63.720

retaining a relatively low TX pulse repetition frequency (PRF), which is on the order of 1350 Hz, the DPC technique [6], [7], [8] is applied through the use of five separate receiving azimuth channels. To simultaneously implement the ScanSAR, SCORE, and DPC techniques, a number of requirements have been considered during the design of the overall radar antenna system. In this work, the radar antenna elevation pattern (whose reconfigurability is needed to implement the ScanSAR and SCORE techniques) is not discussed. Indeed, in the following analysis, we focus our attention only on the azimuth pattern.

In this regard, we note that the five channels required by the DPC configuration of the ROSE-L system are obtained through five adjacent aperture antennas (each of them 2.2 m long) deployed along the flight direction. These five antennas, which hereafter are called panels, separately work in the RX mode, whereas they cooperate in the TX mode behaving as a five-element linear array with an interelement distance of 2.2 m. In particular, according to the current system design, the five separate array elements are excited with equi-amplitude input currents with different phases. In the antenna jargon, this kind of array is named "isophoric" [23].

B. Two-Look ScanSAR Mode Constraints

Starting from the values collected in Table I, setting a sensor velocity $v = 7200$ m/s and a sensor altitude $h = 700$ km, we have applied (2), (3), and (6) obtaining the results reported in Table II, that is, the footprint lengths required to achieve the current ROSE-L system design, for each burst, the one-look, bulk two-look, and full two-look ScanSAR modes, respectively. The azimuth beamwidth values corresponding to the footprint lengths of Table II are reported in Table III, where we account for different angular apertures necessary to achieve the desired footprint length at the far, middle, and near ranges, respectively. In agreement with (2) and (3), the reported values show that to pass from the one-look to full two-look mode, it is basically required a beam-width doubling. Note also that the most critical case, which requires the widest azimuth beam, is represented by

TABLE III
ANTENNA AZIMUTH BEAMWIDTH REQUIRED FOR DIFFERENT ROSE-L SCANSAR MODES

Antenna azimuth beam-width required for the different ROSE-L ScanSAR modes			
	Burst 1 [deg]	**Burst 2** [deg]	**Burst 3** [deg]
One-look mode*	2.3 - 2.4 - 2.5	2.2 - 2.3 - 2.4	2.1 - 2.1 - 2.2
Bulk two-look mode*	3.5 - 3.7 - 3.8	3.3 - 3.4 - 3.5	3.0 - 3.2 - 3.3
Full two-look mode*	4.1 - 4.2 - 4.4	3.8 - 4.0 - 4.1	3.6 - 3.7 - 3.9

*The reported values are relevant to far, middle and near range, respectively, of the corresponding sub-swath.

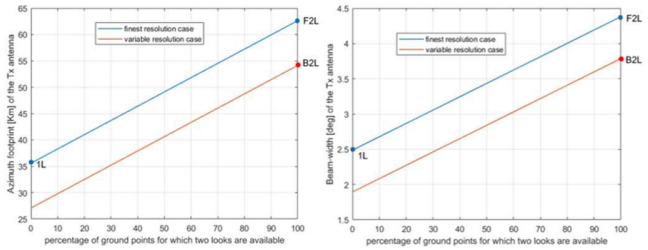

Fig. 4. Relevant to the current ROSE-L antenna system. (Left) Azimuth footprint length versus the corresponding percentage of ground points for which two looks are available with the finest resolution $\Delta x = \Delta x_{\text{full}}$ (blue line) and with resolution $\Delta x \in [\Delta x_{\text{full}}, 2\Delta x_{\text{full}}]$ (red line). The three points 1L, F2L, and B2L in the plots represent the azimuth footprint required to achieve the one-look, full two-look, and bulk two-look modes, respectively. (Right) Same as the left, but for the y-axis, which represents the antenna azimuth beamwidth for the most critical case, that is, burst 1 at the nearest range.

the near range of burst 1. In this case, to achieve the full two-look mode, an azimuth beamwidth of 4.4° is required. From (4) and (7), we have obtained the curves shown in Fig. 4 for azimuth footprints halfway between the one-look and full two-look ScanSAR modes. More specifically, in Fig. 4, left, we plot the azimuth footprint length versus the corresponding percentage of ground points for which two looks are available with the finest resolution $\Delta x = \Delta x_{\text{full}}$ (blue line) and with resolution $\Delta x \in [\Delta x_{\text{full}}, 2\Delta x_{\text{full}}]$ (red line). The three points 1L, F2L, and B2L in the plots indicate the one-look, full two-look, and bulk two-look modes, respectively, as reported in Table II. The beamwidth values corresponding to the footprint lengths of the left of Fig. 4 are plotted, for burst 1 at the nearest range, in the right of the same figure.

To analyze which ScanSAR mode can be achieved with the current ROSE-L system design, we show in Fig. 5 the azimuth cut of the (normalized) two-way pattern obtained through the combination of the TX and RX patterns of the ROSE-L antenna system described above. Moreover, in Fig. 5, we have also marked with red, orange, and green lines the edges of the angular regions required to obtain the one-look, bulk two-look, and full two-look modes, respectively, for the most critical burst (burst 1) at the most critical range (the nearest range), consistently with Table III. Fig. 5 shows that according to the current system design, the ROSE-L system is quite well tailored to the one-look mode. In particular, at the edges of the one-look mode region, we measure a two-way gain decay of 4.9 dB with respect to the maximum gain. Better results are achieved with burst 2 (−4.2 dB) and burst 3 (−2.7 dB), which

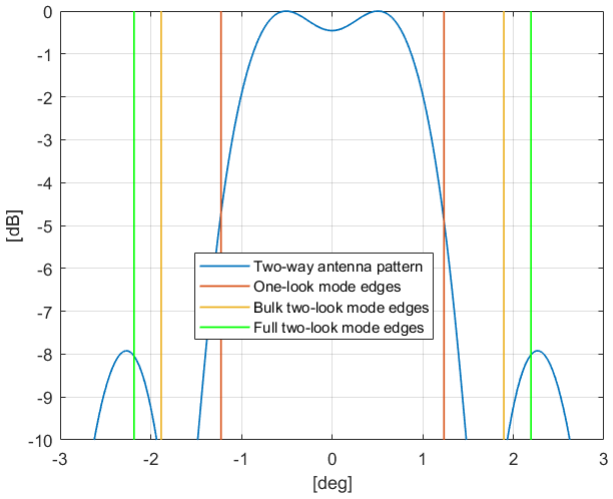

Fig. 5. Relevant to the current ROSE-L antenna system. Azimuth cut of the (normalized) two-way pattern (blue line) with highlighted the edges of the angular regions required to obtain the one-look (red line), bulk two-look (orange line), and full two-look (green line) modes for burst 1 at the nearest range.

are not reported for brevity. Fig. 5 shows also that according to the current system design, neither the full two-look mode nor the bulk two-look mode can be achieved.

IV. ROSE-L Case Study: Preliminary Considerations for the Achievement of Two-Look ScanSAR Mode

Our main goal is to shape the two-way pattern of the ROSE-L antenna system to enable the two-look ScanSAR mode. To this aim, we intend to modify neither the main antenna architecture nor the main system parameters of the current design. More precisely, with respect to the ROSE-L system parameters introduced in Section III, in this study we do not modify:

1) the burst period and duration;
2) the PRF;
3) the properties of the single panel of the TX array;
4) the number and positions of the panels of the TX array.

The aim of the constraint 1) is to retain with the two-look mode the same azimuth resolution of the current ROSE-L system. The constraint 3) implies that we will not act on the RX antenna system (which is represented, for each channel of the DPC configuration, by the single panel of the TX array). Also, we will act neither on the geometry of the TX array (see constraint 4) nor on the geometric as well as electromagnetic properties of the single elements of the TX array (see again constraint 3). Instead, to properly shape the two-way pattern of the ROSE-L antenna system, we intend to act only on the distribution of the input excitations of the five array panels of the TX antenna. To this aim, a proper array synthesis algorithm [9] is necessary. In this regard, to evaluate the performance of the synthesized azimuth pattern, and to properly drive the implementation of the most appropriate synthesis algorithm, several figures of merit can be in principle considered. Among these, hereafter, we focus on the following figures of merit: azimuth beamwidth, relative noise equivalent sigma zero (RNESZ), azimuth ambiguity signal ratio (AASR) and integrated scalloping (IS). In particular, we show how these figures of merit can be translated into optimization constraints for the array synthesis procedure.

The figure of merit related to the azimuth beamwidth is the two-way pattern decay at the edges of the angular region of our interest, that is, the bulk and/or full two-look mode region introduced in Section II. We will account for this figure of merit both during the array synthesis procedure and, a posteriori, when evaluating the performance of the synthesized arrays.

The RNESZ is defined as follows:

$$\mathrm{RNESZ} = \frac{\mathrm{NESZ}_{\mathrm{test}}}{\mathrm{NESZ}_{\mathrm{ref}}} \tag{9}$$

where the subscripts ref and test stand for reference and under test, respectively. In our case, the reference radar is the ROSE-L one employing the original TX array, whereas the radar under test is the ROSE-L one employing the TX array that we propose to synthesize. It is noted that in our case, the only difference between the reference radar and the radar under test is the set of input excitations of the TX array. Accordingly, the RNESZ in (9) simplifies as follows:

$$\mathrm{RNESZ} = \frac{G_{\mathrm{ref}}}{G_{\mathrm{test}}}\frac{P_{\mathrm{ref}}}{P_{\mathrm{test}}} = \frac{1}{\eta_G}\frac{1}{\eta_P} \tag{10}$$

where P and G are the input power and the gain of the considered TX array, respectively. The expression in (10) shows that when reconfiguring the input excitations of the original ROSE-L TX array, two factors contribute to the corresponding modification of the NESZ. The first one ($1/\eta_G = G_{\mathrm{ref}}/G_{\mathrm{test}}$) is the ratio between the gains of the two TX arrays that are compared and thus depends on the considered view angle. It is recalled that in the ROSE-L case, which is currently tailored to the one-look ScanSAR mode, achieving the two-look mode basically requires a beamwidth doubling (see Table III). This leads to a corresponding, unavoidable, antenna gain decrease, whose amount is approximately a factor 2. Thus, the first term in (10) is, in the worst case, unavoidably on the order of 3 dB: this represents the price to be necessarily paid when reconfiguring the input excitations of the original ROSE-L TX array in order to enable the two-look ScanSAR mode. Since the efficiency factor η_G depends on the pattern of the array to synthesize, this factor can be controlled during the array synthesis procedure. Moreover, it will be considered a posteriori when evaluating the performance of the synthesized arrays. The second factor ($1/\eta_P = P_{\mathrm{ref}}/P_{\mathrm{test}}$) in (10) is the ratio between the input powers delivered to the TX arrays. This term is independent of the considered view angle. In our particular case, the reference antenna is the original ROSE-L TX array, which is an isophoric one. Thus, it guarantees an optimal use of the power potentially available at the five array elements since the corresponding five amplifiers operate all at the same, optimal, working point. Differently, if a tapering of the input excitation amplitudes of the array elements is applied, the amplifiers relevant to the five different panels are compelled to operate at different working points, thus

inducing efficiency losses in terms of power delivered to the overall antenna system. Accordingly, in our particular case, the efficiency factor η_P in (10) simplifies as follows:

$$\eta_P = \frac{1}{5}\sum_n \left[\frac{A_n}{\max(A_n)}\right]^2 \tag{11}$$

where 5 is the number of the elements of the array and A_n is the amplitude of the input excitation, say $I_n, = A_n e^{j\phi n}$, of nth element of the considered five-element array. As a matter of fact, when the synthesized array is isophoric, from (11), we obtain $\eta_P = 1$. More generally, when the synthesized array is nonisophoric, we obtain $\eta_P < 1$: the smaller the dynamic of the amplitudes of the input excitations of the synthesized array, the higher the efficiency parameter in (11), and the smaller the corresponding NESZ impairment with respect to the original ROSE-L TX array. Control of the efficiency factor η_P can be pursued during the array synthesis procedure imposing proper constraints on the dynamic of the amplitudes of the input excitations to be calculated. Moreover, this factor will be considered a posteriori when evaluating the performance of the synthesized arrays.

The AASR is defined in [24]. In the ScanSAR case, the AASR depends on the azimuth coordinate of the illuminated target. Numerical results reported in Section V show that this parameter is not particularly critical when moving toward a two-look ScanSAR mode with the ROSE-L system. For this reason, minimization of the AASR will be not pursued during the array synthesis step. In any case, this figure of merit will be considered a posteriori when evaluating the performance of the synthesized arrays.

The IS coefficient is defined as follows:

$$\mathrm{IS}(x) = \frac{1}{x_e - x_s}\int_{x_s}^{x_e} \left|W\left(\varphi\left(x, x'\right)\right)\right| dx' \tag{12}$$

where the typical cylindrical reference system with the axis coincident with the sensor flight direction is considered [12], being x and x' the azimuth coordinates of the considered target and the antenna phase center during the burst acquisition, respectively. Moreover, $W(\cdot)$ is the two-way pattern of the radar antenna; $\phi(x, x')$ is the view angle under which the antenna looks the considered target; and x_s and x_e are the azimuth coordinates of the antenna phase center at the edges of the processed synthetic aperture. Note that in the burst mode case, the IS coefficient in (12) depends on the azimuth coordinate of the illuminated target. Although the meaning of the IS curve is quite intuitive, in Appendix B, we show, through the use of simulated SAR data, that this curve represents an effective figure of merit to measure the performance of the proposed synthesized arrays for what attains the scalloping effect control.

Different processing techniques exist to mitigate the scalloping [25], [26] in burst mode SAR imaging. In addition, hardware strategies may be applied, such as that implemented by the TOPS acquisition mode [18]. Notwithstanding, in the following, we will focus only on the ScanSAR acquisition mode since it will be exploited by the ROSE-L system and, as highlighted above, our aim is not to change the original system design finalized in the past years. For this mode, proper shaping of the two-way pattern may represent a powerful solution to mitigate the scalloping effect. In particular, to mitigate the scalloping, while reducing the computational burden of the synthesis procedure, it is convenient to control secondary figures of merit directly related to the IS coefficient, such as the ripple of the two-way pattern, thus avoiding to compute the integral in (12) when searching the optimal distribution of the input excitations of the five array panels. In any case, the IS coefficient in (12) will be considered a posteriori when evaluating the performance of the synthesized arrays.

V. ROSE-L Case Study: Synthesis of Nonisophoric Arrays Tailored to the Two-Look ScanSAR Mode

Calculation of the input excitations of different panels of the current ROSE-L array to enable the desired two-look ScanSAR mode requires to implement an array synthesis procedure capable, in principle, of simultaneously accounting for all the figures of merit introduced in Section IV. Therefore, we have to address a multiparametric optimization problem, which is not linear, since the relation between the array input excitations' phases (which represent a subset of the unknowns of the problem) and the field radiated by the array is not linear. Moreover, translating some of the figures of merit listed above into mask constraints for the azimuth pattern leads to nonconvex constraints for the optimization problem at hand (consider, for instance, the mask imposed by a possible constraint on the maximum acceptable ripple of the two-way gain, aimed at mitigating the scalloping effect).

Summing up, the array synthesis procedure aimed at achieving the two-look ScanSAR mode with the available TX array structure requires solving a multiparametric, nonconvex optimization problem. Thus, local optimization procedures are not appropriate since they could be trapped in local minima, and the use of global procedures is instead needed. In our case, the number of involved unknowns (five complex input excitations, that is, ten real unknowns) is quite small. Accordingly, we have implemented a synthesis algorithm based on a brute-force exhaustive search (subject to the constraints discussed in Section V-A), which is thus capable of providing a benchmark solution for any other global optimization algorithm at the expenses of the computational efficiency that, however, in our case, does not represent a severe problem.

A. Array Synthesis Algorithm

The implemented array synthesis procedure scans the amplitudes and phases of the input excitations of the five array panels according to the following two constraints, both relevant to the properties of the searched input excitations.

1) Constraint 1: With the aim of reducing even more the number of unknowns (to reduce the involved computational burden), only input excitations that are symmetric (both in amplitude and phase) with respect to that of the central panel are considered. By doing so, the number of unknowns becomes equal to four, once the input excitation of the central panel is fixed. Note that, in principle, such a strategy cuts off possible solutions well-tailored to our case of interest since we are not ensured that the optimal distribution of input

excitations is symmetric with respect to the central element of the array. Some tests not reported here for brevity, however, have confirmed that beamwidths as wide as those required to achieve the desired two-look ScanSAR mode are well-reached when enforcing such a symmetry property on the input excitations.

2) Constraint 2: With the aim of increasing the efficiency η_p in (11), we have enforced a constraint on the maximum allowable dynamic of the amplitudes of the input excitations. In particular, we have enforced a maximum dynamic equal to 1.5.

Summing up, for the central panel, we have set a real and unitary input excitation. For the two unknown complex excitations of the first and second panel, we have scanned 80 amplitude levels in the range [0.8, 1.2] and 200 phase levels in the range $[0, 2\pi]$. By doing so, we have generated a huge number (256×10^6) of solutions, which have been then selected according to the two following additional constraints, both relevant to the properties of the corresponding two-way azimuth patterns.

3) Constraint 3: With the aim of finding a pattern as large as that needed to enable the two-look ScanSAR mode, we have enforced a threshold on the maximum allowable two-way pattern decay at the edge of the two-look mode region.

4) Constraint 4: To limit the scalloping, we have enforced a threshold on the maximum allowable two-way pattern ripple within the one-look mode region. The aim is to find a solution that, although tailored to the two-look mode (see Constraint 3), ensures within the one-look mode region a scalloping mitigation not worse (possibly better) than that achievable with the current set of input excitations of the ROSE-L TX array.

The rationale behind the setting of the thresholds defining Constraints 3 and 4 is addressed in Section V-B.

B. Threshold Setting

To set the threshold that defines Constraint 3, we have measured the two-way pattern decay at the edge of the one-look mode region achieved with the current set of input excitations, which is equal to 4.9 dB (see Section III-B). A slightly severer value (4.7 dB) has been then set as the threshold on the maximum allowable two-way pattern decay at the edge of the bulk two-look mode region for the array to synthesize. By doing so, for the (bulk) two-look mode, we have used the same beamwidth definition (with a tolerance of 0.2 dB) adopted for the one-look mode with the current set of input excitations.

Proper setting of the threshold defining Constraint 4 requires a short discussion. As clarified above, the aim of this constraint is to find, among the solutions tailored to the two-look mode, those allowing performance not worse than that of the current ROSE-L antenna system in terms of scalloping mitigation within the one-look region. In this regard, we recall (see Section III-B and Fig. 5) that within the one-look region, the two-way azimuth pattern of the current ROSE-L system presents a ripple of 4.9 dB (which coincides with the pattern decay at the edge of the one-look region). On the other side, Fig. 5 also shows that within an area corresponding to about 60% of the overall one-look region, the ripple is equal to

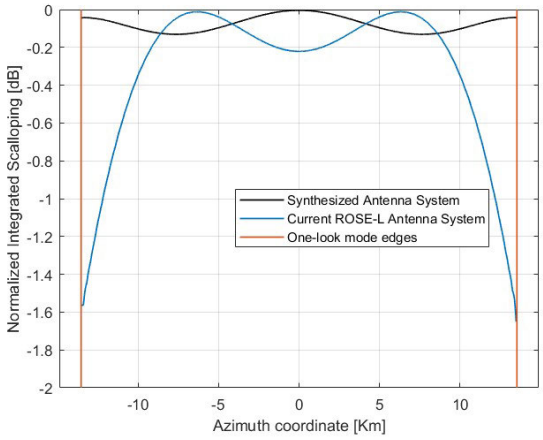

Fig. 6. Scalloping optimization within the one-look region: normalized IS obtained with the synthesized array (black line) and the current ROSE-L array (blue line), with highlighted (red line) the edges of the one-look azimuth region for burst 1 at the nearest range.

only 0.46 dB. Therefore, the current ROSE-L antenna system guarantees a quite good control of the scalloping only within a portion of the entire one-look mode region. This is confirmed by the corresponding IS curve reported in Fig. 6, which is relevant to burst 1 at the nearest range. In Fig. 6, we have highlighted in red the edges of the one-look azimuth region. As it can be seen, with the current ROSE-L antenna system, the IS variation reaches up to 1.65 dB. However, within a region corresponding to about 70% of the one-look region, the maximum IS variation is limited to only 0.22 dB. To get more insights on this topic, in order to find a reasonable threshold for Constraint 4 before embarking in the array synthesis aimed at achieving the two-look mode, we have carried out a preliminary analysis aimed at evaluating the ultimate performance in terms of scalloping mitigation within the one-look region achievable with the ROSE-L antenna architecture. In particular, from the set of 256×10^6 two-way azimuth patterns generated above, we have selected that characterized by the minimum ripple within the one-look mode region. In the following, this solution is named array n.1. The corresponding IS curve is over-plotted in Fig. 6. As it can be seen, acting only on the input excitations of the currently designed array panels, we can obtain within the entire one-look region a maximum IS variation smaller than 0.13 dB, thus improving of 1.52 dB the IS performance of the current ROSE-L antenna system. Moreover, even limiting the comparison only to the central portion of the one-look mode region where the current ROSE-L antenna system guarantees a quite good control of the scalloping, we obtain in any case an improvement of about 0.1 dB. Thus, it is clear that the scalloping mitigation within the one-look region ensured with the current set of input excitations is quite far from the ultimate performance achievable with the same antenna architecture. For this reason, while finding an array solution well-tailored to the two-look mode, within the entire one-look region, we can think to improve the scalloping mitigation capability of the currently designed ROSE-L system.

For the sake of completeness, in Fig. 7, we report the synthesized array input excitations of the synthesized array

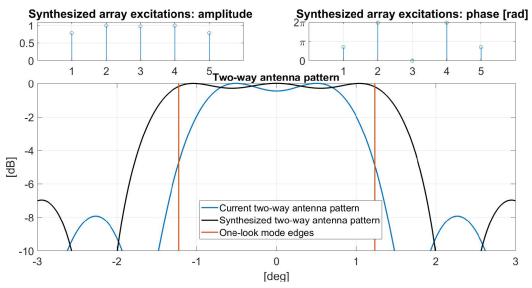

Fig. 7. Scalloping optimization within the one-look region: synthesized array (array n.1). Synthesized input excitations: (top left) normalized amplitude and (top right) phase. (bottom) Azimuth cut of the (normalized) two-way pattern obtained with the synthesized array (black line) and the current ROSE-L array (blue line), with highlighted (red line) the edges of the angular region required to obtain the one-look mode for burst 1 at the nearest range.

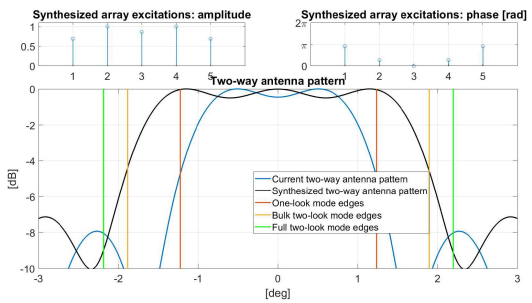

Fig. 8. Two-look mode: synthesized nonisophoric array (array n.2). Synthesized input excitations: (top left) normalized amplitude and (top right) phase. (bottom) Azimuth cut of the (normalized) two-way pattern obtained with the synthesized array (black line) and the current ROSE-L array (blue line), with highlighted the edges of the angular regions required to obtain the one-look (red line), bulk two-look (orange line), and full two-look (green line) modes for burst 1 at the nearest range.

n.1, along with the corresponding azimuth cut of the two-way pattern. For comparison, in Fig. 7, we have also plotted the two-way pattern of the current ROSE-L antenna system; moreover, we have highlighted the edges of the one-look mode for the most critical burst (burst 1) at the most critical range (the nearest range). Note that within the entire one-look region, this optimal two-way pattern presents a ripple of 0.23 dB (see Table IV, which collects the main results relevant to the arrays discussed in this work).

Summing up, considering the ultimate performance in terms of scalloping mitigation achievable with the ROSE-L antenna architecture within the one-look region, the threshold defining Constraint 4 has been set equal to 0.5 dB, that is, about the double of the optimal ripple achievable without enforcing any additional constraint. Note that numerical experiments, not reported here for brevity, show that if we enforce minimization of the ripple within the overall two-look region (rather than the one-look one), we obtain within the one-look region a strong degradation of the ripple with respect to the solution of Fig. 7. For this reason, we decided to give up minimization of the ripple within the overall two-look region, and to search a solution tailored to the two-look mode and capable of outperforming the current ROSE-L antenna system in terms of scalloping mitigation within the one-look region.

C. Results

Starting from the set of 256×10^6 azimuth solutions generated in Section V-A by enforcing Constraints 1 and 2, subsequent enforcement of Constraints 3 and 4 with the thresholds defined in Section V-B has led to a subset of 32 patterns. Among these solutions, we have selected the one that minimizes the maximum RNESZ within the one-look region. In Fig. 8, we report the synthesized array input excitations (top panels), along with the corresponding azimuth cut of the (normalized) two-way pattern. As usual, in Fig. 8, we have also plotted the two-way pattern of the current ROSE-L antenna system; moreover, we have highlighted the edges of the angular regions required to obtain the one-look, bulk two-look, and full two-look modes for burst 1 at the nearest range.

As reported in Table IV, at the edges of the bulk two-look mode region, the two-way gain decay (with respect to the maximum gain) is 4.4 dB, in agreement with the enforced Constraint 3. It is remarked that this value is obtained for burst 1 at the nearest range where, as observed above (see Table III), the azimuth beamwidth required for each considered mode (one-look, bulk two-look, or full two-look) is the widest one. Considering the pattern shape, this case represents the most critical one and for brevity we will focus only on it in the subsequent analysis. By the way, results relevant to the other bursts (at the nearest range) are included in Table IV.

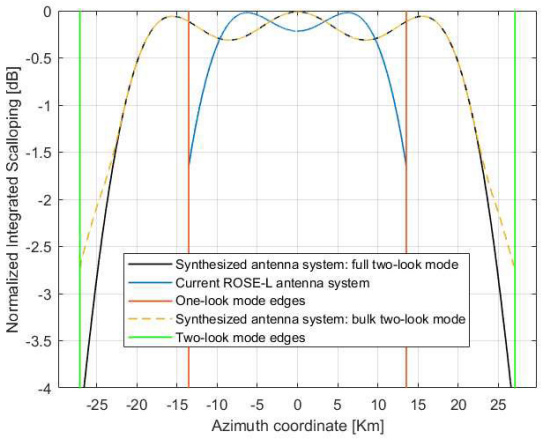

Fig. 9. Relevant to the synthesized nonisophoric array of Fig. 8 (array n.2). Normalized IS obtained with the synthesized array exploiting the full two look-mode (black line), the synthesized array exploiting the bulk two-look mode (orange dashed line), and the current ROSE-L array (blue line). The edges of the one-look (red line) and two-look (green line) azimuth regions for burst 1 at the nearest range are highlighted in the plot.

Turning to the scalloping mitigation, in agreement with the enforced Constraint 4, within the entire one-look region, the synthesized two-way pattern presents a ripple of 0.5 dB, which is 4.3 dB better than that achieved with the current ROSE-L antenna system (see Table IV). In Fig. 9, we show the IS obtained with the synthesized array exploiting the full and the bulk two-look mode, along with the edges of the one-look and two-look azimuth regions. For comparison purposes, in Fig. 9, the IS curve obtained with the current set of input excitations of the ROSE-L array (blue line) is over-plotted. Note that the figures of merit relevant to the original ROSE-L design are hereafter reported only within the one-look region,

TABLE IV
MAIN RESULTS RELEVANT TO THE ALL THE ARRAYS DISCUSSED IN THIS WORK

Main results relevant to the all the arrays discussed in the work							
	Current ROSE-L Array	Array n.1	Array n.2	Array n.3	Array n.4	Array n.5	
Excitations tapering	Isophoric	Non-isoph.	Non-isoph.	Isophoric	Isophoric	Non-isoph.	
η_P	0 dB	-1.40 dB	-1.30 dB	0 dB	0 dB	-0.66 dB	Burst 1 Burst 2 Burst 3
Worst η_G within the 1LR	-	-2.54 dB	-3.20 dB	- 3.75 dB	-3.2 dB	-2.63 dB	Burst 1 Burst 2 Burst 3
WRNESZ within the 1LR	-	3.94 dB	4.50 dB	3.75 dB	3.2 dB	3.29 dB	Burst 1 Burst 2 Burst 3
2WPD @ B2LRE	-	6.46 dB 3.94 dB 2.71 dB	4.4 dB 2.6 dB 1.8 dB	7.14 dB 3.89 dB 2.45 dB	4.5 dB 2.4 dB 1.5 dB	5.2 dB 3.0 dB 2.0 dB	Burst 1 Burst 2 Burst 3
2WPD @ F2LRE	-	13.95 dB 10.00 dB 7.48 dB	8.9 dB 6.7 dB 5.2 dB	27.12 dB 13.03 dB 8.62 dB	12.3 dB 7.6 dB 5.6 dB	12.6 dB 8.4 dB 6.1 dB	Burst 1 Burst 2 Burst 3
Ripple within the 1LR	4.9 dB 4.2 dB 2.7 dB	0.23 dB	0.5 dB	0.82 dB	1.14 dB	0.52 dB	Burst 1 Burst 2 Burst 3
MISV within the 1LR	1.65 dB	0.13 dB	0.31 dB	0.53 dB	0.77 dB	0.33 dB	Burst 1 Burst 2 Burst 3
MISV within the 2LR (bulk)	-	4.2 dB 2.4 dB 1.5 dB	2.9 dB 1.5 dB 0.9 dB	4.1 dB 2.0 dB 1.1 dB	2.6 dB 1.2 dB 0.8 dB	3.2 dB 1.7 dB 0.9 dB	Burst 1 Burst 2 Burst 3
MISV within the 2LR (full)	-	6.4 dB 4.3 dB 2.9 dB	4.5 dB 3.0 dB 1.9 dB	7.3 dB 4.4 dB 2.6 dB	4.76 dB 2.82 dB 1.62 dB	5.3 dB 3.4 dB 2.1 dB	Burst 1 Burst 2 Burst 3
WAASR within the 1LR	-31.4 dB -32.2 dB -33.9 dB	-29.8 dB -30.5 dB - 32.2 dB	-29.7 dB -30.4 dB -32.0 dB	-29.6 dB -30.3 dB -31.93 dB	-29.5 dB -30.2 dB -31.8 dB	-28.7 dB - 30.4 dB - 32.0 dB	Burst 1 Burst 2 Burst 3
WAASR within the 2LR (bulk)	-	-16.8 dB - 19.6 dB - 21.4 dB	-17.2 dB -19.8 dB -21.5 dB	-16.6 dB -19.6 dB -21.5 dB	-17.2 dB -19.9 dB -21.7 dB	- 17.1 dB -19.8 dB -21.5 dB	Burst 1 Burst 2 Burst 3
WAASR within the 2LR (full)	-	-14.6 dB -17.1 dB - 18.8 dB	-15.0 dB -17.3 dB -18.9 dB	- 14.2 dB -17.0 dB -18.77 dB	- 14.8 dB - 17.3 dB -19.0 dB	-14.8 dB -17.3 dB -18.9 dB	Burst 1 Burst 2 Burst 3

The array solutions highlighted in green are tailored to the one-look ScanSAR mode. Notwithstanding, for the sake of completeness, the array parameters of the synthesized arrays n.1 and n.3 are reported also with respect to the two-look ScanSAR mode.

Legend.
WRNESZ: Worst Relative NESZ
2WPD: Two-way pattern decay
B2LRE: Bulk Two-Look Region Edge
F2LRE: Full Two-Look Region Edge
1LR: One-Look Region Border,
2LR: Two-Look Region Border
MISV: Maximum Integrated Scalloping Variation
WAASR: Worst AASR

for which the system has been designed. Within the one-look region, the maximum IS variation is equal to 0.31 dB, that is, 1.34 dB better than the maximum IS variation achieved with the current set of array input excitations (see Table IV). This means that if we limit the analysis only to the one-look mode region (to which the original ROSE-L antenna is tailored), the synthesized array (which is tailored to the two-look mode) allows a much better control of the scalloping effect with respect to the original ROSE-L antenna. Outside the one-look region, with the synthesized array, if we exploit the bulk

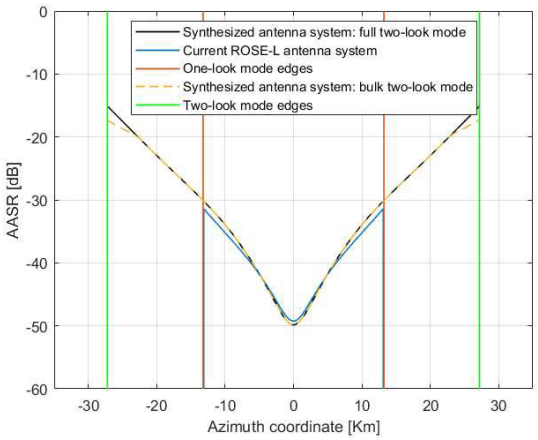

Fig. 10. Relevant to the synthesized nonisophoric array of Fig. 8 (array n.2). AASR obtained with the synthesized array exploiting the full two look-mode (black line), the synthesized array exploiting the bulk two-look mode (orange dashed line), and the current ROSE-L array (blue line). The edges of the one-look (red line) and two-look (green line) azimuth regions for burst 1 are highlighted in the plot.

two-look mode, the maximum IS variation within the two-look region is 1.2 dB worse than that obtained with the current ROSE-L antenna system within the one-look region (see again Table IV). It is noted that the maximum IS variation occurs at the edges of the two-look region, where the IS rapidly decreases. An increase of the sensor-to-target distance, which involves a reduction of the azimuth beamwidth required for the (bulk/full) two-look mode, would thus lead to a corresponding reduction of the maximum IS. Therefore, also for the IS, the nearest range of the first burst (considered in Fig. 9) represents the worst case. Results relevant to the other bursts (at the nearest range) are in any case included in Table IV.

The AASR curves obtained with the synthesized array exploiting the full two-look mode and the bulk two-look mode are plotted in Fig. 10 along with that of the current ROSE-L array. It is noted that with the synthesized array, we achieve within the one-look mode region practically the same AASR performance of the original ROSE-L antenna system. Moreover, the AASR of the synthesized array is lower than -20 dB in a great part of the two-look mode region, reaching higher values only at the very edges of this region. Therefore, also for the AASR, the nearest range of the first burst (considered in Fig. 10) represents the worst case since the increase of the sensor-to-target distance involves reduction of the azimuth beamwidth required for the two-look modes. The results relevant to the other bursts are in any case reported in Table IV. The RNESZ achieved with the synthesized array is not plotted here for brevity (in any case, it is plotted for comparison purposes in Section VII). As expected, the NESZ of the synthesized array is mainly worse than that of the original ROSE-L antenna system, with a difference that in the worst case reaches 4.5 dB. As a matter of fact, only at the very edges of the one-look region, the RNESZ becomes negative. As clarified above, most of this NESZ increment is unavoidable and represents the price to be paid to reconfigure a system tailored to the one-look ScanSAR mode to enable the two-look ScanSAR mode. In particular, in the worst case, the efficiency factor η_G in (10) is equal to -3.2 dB, which is quite close to the -3 dB value roughly expected. Moreover, the efficiency factor η_P in (10) and (11) is equal to 0.74 (that is, -1.3 dB). In this regard, we remark that the obtained amplitudes' dynamic of the input excitations is equal to the maximum threshold (1.5) that we have enforced as a constraint of the synthesis algorithm. This means that to achieve the desired beam enlargement necessary for the two-look mode, the synthesis algorithm, besides a phase tapering of the input excitations, has exploited as much as possible the available (although constrained) degrees of freedom on the amplitude of the input excitations. In other words, the constraint on the amplitudes' dynamic of the input excitations turned out to be effective during the optimization process carried out by the synthesis algorithm, thus cutting off solutions more performing in terms of figures of merit other than the efficiency factor η_P in (11). This means that when acting on the reduction of the RNESZ by enforcing this kind of constraint on the input excitations, impairment of the pattern performance (in terms of ripple and/or gain decay at the edges of the two-look region) must be unavoidably expected.

VI. ROSE-L Case Study: Synthesis of Isophoric Arrays Tailored to the Two-Look ScanSAR Mode

To increase the efficiency η_P in (11), we have slightly modified the synthesis scheme of Section IV by limiting our search to the isophoric arrays. To do this, we made Constraint 2 more stringent by enforcing equi-amplitude input excitations, thus constraining our solution to reach $\eta_P = 1$. As clarified above, we expect that this involves an impairment of the pattern performance with respect to the nonisophoric solution obtained in Section V. For this reason, it is convenient to relax at least one among Constraints 3 and 4.

With reference to Constraint 4, to set a proper threshold for the case at hand, we have followed the same rationale of the procedure described in Section V-B, that is, we have calculated the optimal equi-amplitude input excitations that allow minimization of the ripple within the overall one-look region, without enforcing any other pattern constraint outside this region. With the synthesized isophoric array, which in the following is named array n.3, we obtained a two-way pattern (not plotted for brevity) with a ripple of 0.81 dB within the one-look region. As expected, this value is worse than that achieved with the optimal nonisophoric array n.1. Following the rationale of the previous section, the threshold defining Constraint 4 has been set equal to about the double of the ripple of the optimal isophoric array n.3, which is 1.5 dB.

Note that with respect to the procedure of Section IV, we have reduced even more the number of unknowns since now, the amplitudes of the input excitations are not unknown anymore. In particular, by retaining Constraint 1, we have reduced the number of unknowns to just two, that is, the two real excitation phases of the first and second array panels. For this reason, without increasing the computational burden of the optimization procedure, we have scanned a number (720) of phase levels of the input excitations greater than that (200) considered in Section IV. By doing so, we have generated 518.4×10^3 solutions; subsequent enforcement of

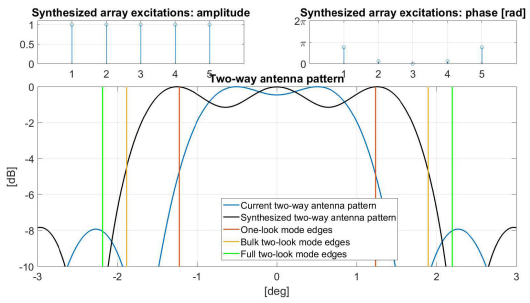

Fig. 11. Two-look mode: synthesized isophoric array (array n.4). Synthesized input excitations: (top left) normalized amplitude and (top right) phase. (bottom) Azimuth cut of the (normalized) two-way pattern obtained with the synthesized array (black line) and the current ROSE-L array (blue line), with highlighted the edges of the angular regions required to obtain the one-look (red line), bulk two-look (orange line), and full two-look (green line) modes for burst 1 at the nearest range.

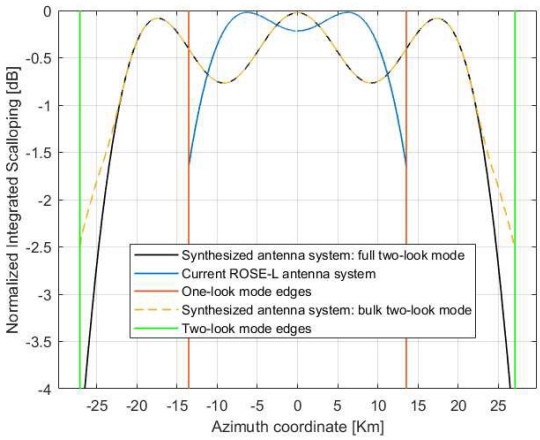

Fig. 12. Relevant to the synthesized isophoric array of Fig. 11 (array n.4). Normalized IS obtained with the synthesized array exploiting the full two look-mode (black line), the synthesized array exploiting the bulk two-look mode (orange dashed line), and the current ROSE-L array (blue line). The edges of the one-look (red line) and two-look (green line) azimuth regions for burst 1 at the nearest range are highlighted in the plot.

Constraints 3 and 4 has then led to a subset of 670 patterns. Among these solutions, as in Section V, we have selected the one that minimizes the maximum RNESZ within the one-look region. In Fig. 11 (top), we report the synthesized array input excitations. In Fig. 11 (bottom), it is plotted the corresponding azimuth cut of the (normalized) two-way pattern, along with the (normalized) two-way pattern of the current ROSE-L antenna system, as well as the edges of the angular regions of our interest for the most critical case, that is, burst 1 at the nearest range. In this case, in agreement with the enforced Constraint 3, at the edges of the bulk two-look mode region, we obtain a two-way gain decay of 4.5 dB. At the edges of the full two-look mode region, the two-way gain decay is considerably worse than that achieved with the nonisophoric array n.2 (see Table IV, which collects the results relevant to all the bursts at the nearest range).

Still focusing on the nearest range of burst 1, in agreement with the enforced Constraint 4, within the entire one-look region, the synthesized two-way pattern presents a ripple of 1.14 dB, which is 0.64 dB worse than that achieved with the nonisophoric array n.2. In any case, the ripple of this synthesized isophoric solution is lower (3.76 dB) than that achieved with the current ROSE-L antenna system. In Fig. 12, we report the IS curves obtained with the synthesized array and that obtained with the current ROSE-L array. For burst 1 at the nearest range, within the one-look region, the maximum IS variation is 0.46 dB worse than that achieved with the non-isophoric array n.2, and 0.88 dB better than the maximum IS variation achieved with the current ROSE-L antenna system. The results achieved outside the one-look region are collected in Table IV, which reports, as usual, also the performance relevant to the other bursts.

The AASR curves obtained with the synthesized array are very similar to those of the isophoric array n.2; therefore, they are not plotted for brevity. Synthetic results are in any case summarized, as usual, in Table IV.

Also the RNESZ curve achieved with the synthesized array is not plotted here (it is plotted for comparison purposes in Section VII. In any case, we remark that for the most critical case, which is burst 1 at the nearest range, the RNESZ becomes negative within a portion that now is the 16% of the one-look region. Moreover, the mean level of the RNESZ has dropped about 1.3 dB with respect to the corresponding curve relevant to the nonisophoric array n.2. It is also noted that this difference is totally due to the adoption of equi-amplitude input excitations, leading to $\eta_P = 1$. Indeed, in the worst case, the efficiency factor η_G in (10) is now equal to -3.2 dB, that is, the same value obtained with the isophoric array n.2.

VII. Discussion

A discussion on the solutions shown above is now in order.

The nonisophoric array n.2 outperforms the isophoric array n.4 in terms of figures of merit related to the pattern shape. On the other side, the NESZ curve of the array n.4 is lower than that of the array n.2. This is because the isophoric arrays guarantee an optimal exploitation of the power potentially available at different array panels. In this regard, it is worth stressing that the synthesized arrays n.2 and n.4 are optimal according to optimization metrics that we judged particularly relevant. Obviously, enforcement of constraints other than those used in Sections V and VI would have led to different solutions, optimal with respect to metrics different from the adopted ones, and in principle still suitable for a two-look ScanSAR configuration. In other words, we stress that the two solutions presented in Sections V and VI represent just two samples of a wide family of potential solutions well-tailored to our scopes. To better clarify this point, we have carried out a massive analysis on the nonisophoric solutions potentially tailored to the two-look ScanSAR mode. More specifically, we started from the set of 256×10^6 nonisophoric solutions obtained by enforcing Constraints 1 and 2 as defined in Section V. Then, we relaxed both Constraints 3 and 4. In particular, the threshold on the maximum allowable two-way pattern decay at the edges of the bulk two-look region (Constraint 3) has been set equal to 5.7 dB, whereas the threshold on the maximum ripple within the one-look mode

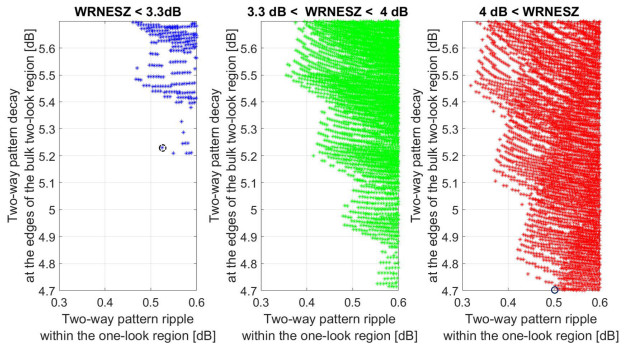

Fig. 13. Relevant to the synthesis of nonisophoric arrays tailored to the two-look ScanSAR mode with the ROSE-L system. Performance analysis of a subset of about 20×10^3 patterns generated with the synthesis algorithm of Section V according to the constraints defined in Section VII. Each plot shows the two-way pattern decay at the edges of the bulk two-look region versus the two-way pattern ripple within the one-look region. The solutions are split into three different panels according to WRNESZ calculated within the one-look region. The arrays n.2 and n.5 are circled in the right and left panels, respectively.

region (Constraint 4) has been set equal to 0.6 dB. By doing so, we have obtained a subset of about 20×10^3 patterns. The performance of all these isophoric solutions, in terms of the figures of merit introduced in Section IV, are summarized in the three plots of Fig. 13 (which refer, as usual, to the worst case, that is, burst n.1 at the nearest range). Note that according to the results shown in Sections V and VI, the AASR has been not considered in this analysis since it turned out to be not particularly critical. As for the other three figures of merit of Section IV, Fig. 13 reports, for all the selected solutions, the two-way pattern decay at the edges of the bulk two-look region versus the maximum ripple within the one-look mode region. Moreover, the solutions have been categorized into three different classes, depending on the worst RNESZ (WRNESZ) calculated within the one-look region. In particular, in the right plot, we have reported the solutions with the worst performance in terms of RNESZ, whereas in the left plot those with the best performance. In the central panel, we have reported the solutions with RNESZ performance lying halfway between the left and right panels. Note that the solutions close to the bottom-left corner of each plot are the most performing in terms of two-way pattern figures of merit since they allow reducing the ripple in the one-look region while guaranteeing a wider beam tailored to the two-look scenario.

The three plots clearly show the tradeoffs related to the optimal choice of the pattern tailored to the two-look ScanSAR mode. For instance, they show that the reduction of the two-way pattern ripple typically involves the increase of the gain decay at the edges of the two-look mode region. Also, the price to be paid to improve the pattern performance is the increase of the RNESZ. As a matter of fact, the nonisophoric solution found in Section V (array n.2) belongs to the right plot (circled red star in the plot). We observe that the two-way pattern ripple within the one-look region achieved with array n.2 can be further improved; however, this involves impairment of the two-way pattern decay at the edges of the two-look region. Indeed, in the three plots of Fig. 13, all the solutions lying on the left of array n.2 do not fulfill Constraint 3 as defined

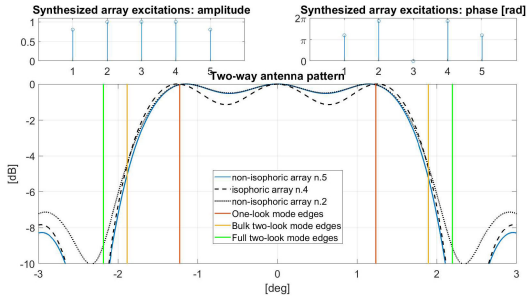

Fig. 14. Two-look mode: synthesized nonisophoric array (array n.5). Synthesized input excitations: (top left) normalized amplitude and (top right) phase. (bottom) Azimuth cut of the (normalized) two-way pattern obtained with array n.5 (blue line), array n.2 (black dotted line), and array n.4 (black dashed line), all exploiting the bulk two-look mode. As usual, the edges of the angular regions required to obtain the one-look (red line), bulk two-look (orange line), and full two-look (green line) modes for burst 1 at the nearest range are highlighted in the plot.

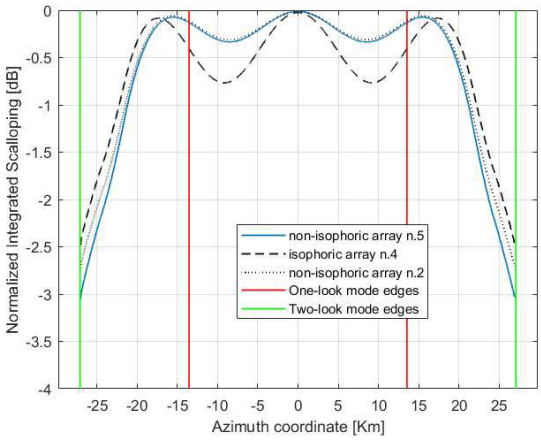

Fig. 15. Normalized IS obtained with array n.5 (blue line), array n.2 (black dotted line), and array n.4 (black dashed line), all exploiting the bulk two-look mode. The edges of the one-look (red line) and two-look (green line) azimuth regions for burst 1 at the nearest range are highlighted in the plot.

in Section V. Also, solutions with RNESZ performance better than that of array n.2 can be found in the central and left plots: however, they show worse performance in terms of two-way pattern figures of merit. In other words, the three plots of Fig. 13 provide dimensioning curves that can drive the choice of the optimal pattern according to the values of the figures of merit that one considers more relevant. To better clarify this aspect, from the huge number of solutions collected in Fig. 13, we have picked up one from the left panel (circled blue star in the plot). This solution, which in the following is named array n.5, combines the strengths of the nonisophoric array n.2 and the isophoric array n.4. To better show this, in Fig. 14 (bottom), we plot the azimuth cut of the (normalized) two-way pattern achieved with this nonisophoric array n.5, the nonisophoric array n.2, and the isophoric array n.4. In Fig. 14 (top), we report the input excitations of the synthesized array n.5. Moreover, for comparison purposes, the IS and RNESZ curves relevant to these three synthesized arrays are plotted in Figs. 15 and 16, respectively. Synthetic results relevant to array n.5 are reported as usual in Table IV. Here, we just stress that this solution represents a very good compromise between the two solutions found in Sections V and VI. Indeed,

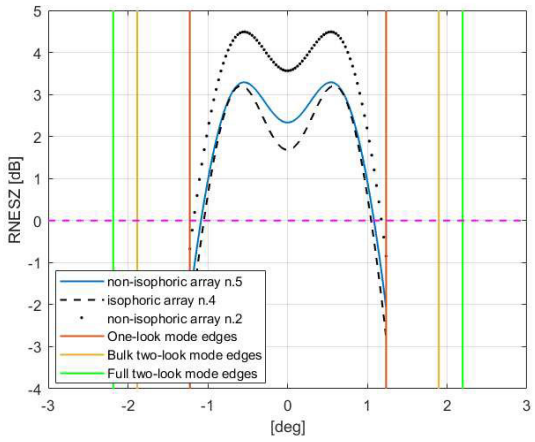

Fig. 16. RNESZ of array n.5 (blue line), array n.2 (black dotted line), and array n.4 (black dashed line). The plot reports the edges of the angular regions required to obtain the one-look (red line), bulk two-look (orange line), and full two-look (green line) modes for burst 1 at the nearest range.

it allows guaranteeing pattern figures of merit comparable to those of the nonisophoric array n.2, while reaching an RNESZ value very close to that of the isophoric array n.4 (see Fig. 16). It is noted that two factors contribute to this notable improvement of the RNESZ curve. First, the efficiency factor η_P in (10) and (11) is now equal to 0.86, that is, -0.66 dB. It is remarked that this value is significantly better (of 0.64 dB) than the analogous one (-1.30 dB) of the nonisophoric array n.2. Indeed, array n.5 exploits a very marginal tapering of the amplitudes of the input excitations (compare the top-left plots of Figs. 8 and 14). As a matter of fact, this reduced exploitation of the available degrees of freedom on the input excitations is paid in terms of two-way decay at the edges of the bulk two-look region, which is now 0.8 dB worse than that achieved with the nonisophoric array n.2. In turn, the maximum IS variation at the edges of the two-look region increases with respect to both array n.2 and array n.4 (see Table IV and Fig. 15). Note, moreover, that in this case, the two-way pattern decay at the edges of the bulk two-look region is only 0.3 dB worse than the two-way pattern decay achieved at the edges of the one-look mode region with the original set of input excitations of the ROSE-L system. Second, the efficiency factor η_G in (10), computed as usual in the worst case, is now equal to -2.63 dB, which is significantly higher than that of the nonisophoric array n.2 and the isophoric array n.4 (in both cases, we measured -3.2 dB, see Table IV). This is due to three features of the obtained two-way pattern. First, the slight beamwidth reduction (testified by the increase of the pattern decay at the edges of the two-look region discussed above), with respect to the patterns of the array n.2 and n.4. Second, the significant reduction of the ripple with respect to the pattern of array n.4: as reported in Table IV, this value is now equal to 0.52 dB (see Fig. 14), which is practically the same as that achieved with array n.2. Third, the reduction of the level of the first sidelobe, especially with respect to the pattern of array n.2 (see again Fig. 14).

Summing up, to achieve array n.5, we slightly relaxed Constraints 3 and 4 in Section V. In particular, we gave up to obtain at the edges of the bulk two-look region a two-way pattern decay better than that measured with the current ROSE-L system at the edges of the one-look region. By doing so, we found a nonisophoric solution that, overall, seems the best candidate to enable the two-look ScanSAR mode with the ROSE-L system.

VIII. Conclusion

This work shows that additional ScanSAR capabilities with respect to those achievable through the current ROSE-L system design can be easily obtained by retaining the same system parameters, such as the geometrical resolution and the swath width and without upsetting the currently designed antenna architecture. Indeed, by acting only on the input excitations of the five elements of the current ROSE-L TX array antenna, we can shape the TX azimuth beam to move from a one-look ScanSAR configuration, for which the ROSE-L system is currently designed, to a two-look one.

Several applications (one of which, relevant to the North–South surface deformation component retrieval, has been analyzed in Appendix A) can take benefit from this additional ScanSAR capability, which, however, cannot be achieved at zero cost. Indeed, the two-look mode requires to double the azimuth beamwidth with respect to the one-look mode, thus leading to an unavoidable antenna gain decrease, whose amount is of approximately 3 dB. This produces an analogous reduction of the power received onboard by the radar, thus mostly impacting the NESZ parameter.

To calculate the array input excitations enabling the desired two-look ScanSAR mode, we have implemented an array synthesis algorithm based on a brute-force exhaustive search, which takes benefit from the very reduced number of unknowns involved in the problem at hand. A number of figures of merit have been introduced with a twofold aim. Some of them have been indeed exploited by the synthesis algorithm to select the most appropriate solution; all of them have been used a posteriori to evaluate the performance of the synthesized arrays.

The main structure of the exploited synthesis procedure is quite flexible. For instance, it allows enforcing a constraint on the maximum acceptable dynamic of the amplitudes of the searched input excitations, with the aim of guaranteeing a better exploitation of the power (potentially) available at different array panels. With the same aim, the synthesis scheme can be tuned in order to reduce the search space only to the class of isophoric arrays. Although the synthesis procedure has been primarily designed to find a set of input excitations well-tailored to a two-look ScanSAR scenario, it can be exploited also to find solutions well-tailored to the one-look scenario. Indeed, with the proposed algorithm, as side result, we have also found the ultimate performance in terms of ripple reduction within the one-look ScanSAR region achievable with the current ROSE-L array structure by acting only on the input excitations. These obtained optimal solutions (particularly, the nonisophoric array n.1) shows that with the current set of input excitations, the ROSE-L system, although designed for a one-look scenario, is quite far from the ultimate achievable performance in terms of scalloping mitigation within the one-look region. According to this result,

we have then focused our synthesis strategy on finding a solution well-tailored to the two-look ScanSAR mode and such to ensure within the one-look mode region a better scalloping mitigation than that achieved with the currently designed ROSE-L system. More generally, we have searched solutions that, within the one-look region, behave not worse than the currently designed ROSE-L system also with respect to the other identified figures of merit. By following this rationale, we have found two solutions tailored to the two-look ScanSAR mode: the nonisophoric array n.2 and the isophoric array n.4, which are characterized by contrasting performance. In particular, the isophoric solution n.4 behaves worse in terms of figures of merit related to the pattern shape, while ensuring a better exploitation of the power available at different array panels. Moreover, within the one-look region, the nonisophoric array n.2 allows us to obtain a ripple control (which means scalloping mitigation) much better than that achieved with the current set of input excitations (tailored to the one-look mode).

To find a solution capable of combining the strengths of the arrays n.2 and n.4, for array n.5 we have slightly relaxed the constraints enforced to obtain these two solutions, carrying out an analysis on the nonisophoric solutions potentially tailored to the two-look ScanSAR mode. In particular, we gave up to obtain at the edges of the bulk two-look region a two-way pattern decay better than that measured with the current ROSE-L system at the edges of the one-look region. By doing so, we found a nonisophoric solution that behaves very close to the array n.2 in terms of pattern figures of merit while showing an NESZ curve very close to that of array n.4. For this reason, the nonisophoric array n.5 seems the best candidate to enable the two-look ScanSAR mode with the ROSE-L system.

For each synthesized array, the performance has been extensively analyzed in the worst case, that is, for burst 1 at the nearest range: the considered figures of merit indeed improve when increasing the elevation angle. Accordingly, one can think to pursue the desired two-look mode in a hybrid way, that is, by accepting to obtain the bulk two-look mode just for the range swath portion relevant to the first burst (or a part of it, for instance, at its mid-range) and the full two-look mode for the remaining portion of the overall range swath.

We further highlight that this article deals with a conceptual performance analysis, not with a technological implementation; evaluation of errors related to the latter issues are, thus, beyond the scope of this work, but they are worth to future analysis.

It is finally remarked that the results of this study, although tailored to the ROSE-L case, can be extended to other systems and thus represent a valuable tool for the design of future SAR missions. In this regard, further investigation of the proposed solutions through in-orbit experiments would be particularly relevant.

Appendix A

As mentioned in Section II, the two-look ScanSAR acquisition mode shows a capability particularly attractive for the application of the DInSAR technique. Indeed, DInSAR measurements allow us to retrieve (with accuracy on the order of fractions of the carrier wavelength) the line of sight component of the surface deformation field that occurred in the illuminated area. Accordingly, to retrieve the overall 3-D deformation field that occurred in the observed area, at least three independent DInSAR measurements are necessary.

As for the East–West and vertical components of the observed deformation field, the benefit can be taken from the (almost) polar orbits followed by the spaceborne SAR sensors. More specifically, the proper combination of the DInSAR measurements relevant to the same area and obtained from ascending and descending orbits allows retrieving at a global scale such deformation components [27]. Unfortunately, this procedure cannot be applied to retrieve with acceptable accuracy the North–South deformation component since the radar line-of-sight is almost orthogonal to the North–South direction, especially for standard SAR acquisitions carried out routinely with no squint angles.

The North–South deformation component can be instead measured by exploiting the acquisition mechanism peculiar of the SAR modes, such as ScanSAR or TOPS, which allow illuminating the same area from different squint angles. Indeed, this procedure, named "burst overlap interferometry" [21], is based on the proper combination of the DInSAR measurements relevant to the overlapping ground areas shared by adjacent bursts. It is stressed that with the currently operative Sentinel-1 TOPS spaceborne systems (for which the full or even the bulk two-look modes are far from being guaranteed [21]), the North–South deformation component can be measured only for a very reduced percentage of the illuminated areas. Achievement of the two-look ScanSAR mode would allow instead to retrieve on a global scale the North–South component of the deformation phenomena occurring on the Earth surface.

The theoretical accuracy of the measurement of the North–South deformation component, through the burst overlap interferometry technique, depends on different factors, such as the azimuthal angular diversity between the overlapping images relevant to the adjacent bursts, the interferometric coherence of the available DInSAR interferograms, and the number of pixels involved in possible spatial averaging procedures. The analytical expression of such accuracy, say $\varepsilon_{\mathrm{NS}}$, can be found in [21]

$$\varepsilon_{\mathrm{NS}} \approx \frac{\lambda}{4\pi}\frac{r}{\Delta_{\mathrm{burst}}}\frac{\sqrt{1-\gamma^2}}{\gamma}\frac{1}{\sqrt{N_L}} \tag{13}$$

where, as usual, r is the range coordinate, λ is the carrier wavelength, and Δ_{burst} is the space period associated with the burst time period . Moreover, γ is the interferometric coherence of the available DInSAR interferograms, and N_L is the number of pixels used in the spatial averaging.

Based on the expression in (13), a straightforward sensitivity analysis tailored to the ROSE-L system parameters reported in Section III is now addressed. In this regard, note that, according to (13), the most critical case is represented by the farthest range of the overall range swath. For this reason, we consider burst 3 at the farthest range and show in Fig. 17 the behavior of this accuracy as a function of the coherence of the DInSAR interferograms used to implement the technique. As it can be seen, in this worst case, with an interferometric coherence

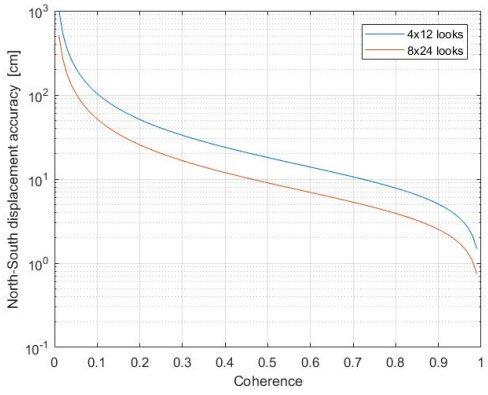

Fig. 17. Theoretical accuracy of the North–South deformation component measurement achievable with the two-look ScanSAR mode of the ROSE-L system (burst 3 at the farthest range) through the burst overlap interferometry, as a function of the DInSAR interferogram coherence. Blue line: accuracy obtained when exploiting 4 × 12 pixels to carry out the spatial averaging aimed at reducing the noise level. Red line: accuracy obtained when exploiting 8 × 24 pixels to carry out the spatial averaging aimed at reducing the noise level.

greater than 0.7, 48 looks (achieved with 4 × 12 pixels spatial averaging) are enough to ensure an accuracy on the order of 10 cm. We further highlight that with the L-band, it is very likely that relatively high values of the coherence can be typically achieved.

APPENDIX B

In this appendix, we show that the IS curve represents an effective figure of merit to measure the performance of the synthesized arrays in terms of scalloping effect control.

To this aim, we have developed a time-domain simulator of ScanSAR raw data and tailored it to the ROSE-L acquisition geometry. In particular, we have simulated the raw data acquired by the system equipped with the currently designed array and with one array synthesized in the work, namely, array n.1 (that is, the array obtained to achieve the scalloping optimization within the one-look mode region). The simulated raw data have been then focused with a common ScanSAR processor.

As the first experiment, we have considered a scene consisting of five pointlike scatterers placed at the nearest range of burst 1 over an absorbing background. The azimuth positions of the targets have been set as follows: one target is located at the center of the burst; two targets near to the one-look mode edges (specifically, ±13.2 km from the burst center); and two targets ±6 km from the burst center. The azimuth cut of the (amplitude of) two obtained focused images (in correspondence with the range position of the five considered targets) is plotted in the two panels of Fig. 18. Comparison between the top panel (relevant to the data acquired with the current ROSE-L antenna system) and the bottom one (relevant to the data acquired with the proposed array n.1) clearly shows different amount of the scalloping in the two considered cases. Note, moreover, that, as expected, the amplitude modulation shown in the two plots (that is, the scalloping) fits very well

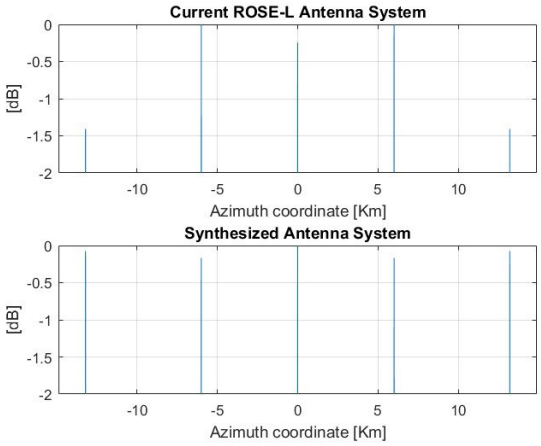

Fig. 18. Evaluation of the scalloping effect through the point target analysis of simulated ROSE-L SAR data. The five considered targets are placed at the nearest range of burst 1, and the azimuth extension of the considered scene coincides with the corresponding one-look region. Amplitude of the focused images relevant to the data acquired by the system equipped (top) with the currently designed array and (bottom) with the proposed array n.1.

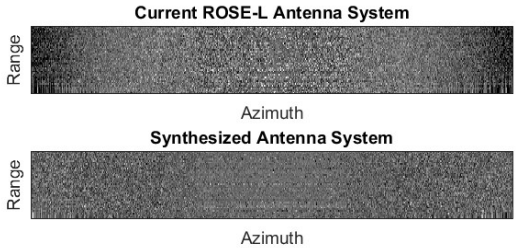

Fig. 19. Evaluation of the scalloping effect through the extended scene analysis of simulated ROSE-L SAR data. The illuminated area has a range extension of 450 m (in the near range region of burst 1) and an azimuth extension coincident with the one-look region of the same burst. Amplitude of the focused images relevant to the data acquired by the system equipped (top) with the currently designed array and (bottom) with the proposed array n.1. A multilook of 2 × 10 in range and azimuth, respectively, has been applied.

the two IS curves of Fig. 6, which are relevant to the two arrays considered in this appendix.

As a second experiment, we have considered an extended scene with flat topography and a reflectivity map computed according to [12]. The illuminated area has a range extension of 450 m (in the near range region of burst 1) and an azimuth extension coincident with the one-look region of burst 1. The amplitude of the two obtained focused images is shown in the two panels of Fig. 18. Note also that a multilook of 2 × 10 in range and azimuth, respectively, has been applied for a final resolution of about 10 m in both directions.

Also in this case, the comparison between the top panel (relevant, once again, to the data acquired with the current ROSE-L antenna system) and the bottom one (relevant, once again, to the data acquired with the array n.1) clearly shows different amounts of the scalloping in the two considered cases. For both amplitude images of Fig. 19, we have carried out the mean along the range direction. The two obtained curves are plotted in Fig. 20. It can be noted that they are practically coincident with the two IS curves of Fig. 6, which, as observed above, are relevant to the two arrays considered in this appendix.

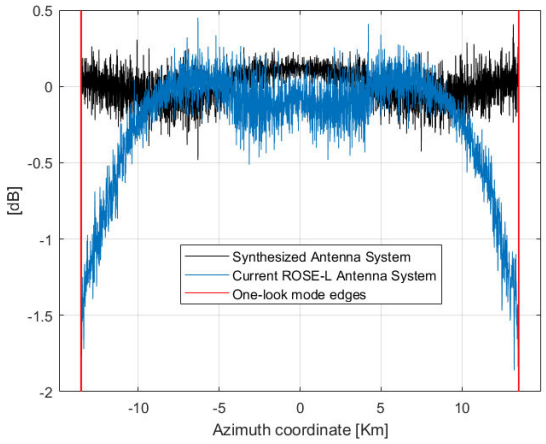

Fig. 20. Evaluation of the scalloping effect through the extended scene analysis of simulated ROSE-L SAR data. Mean (along the range direction) of the two amplitude images of Fig. 19. The blue line is relevant to the currently designed array, the black line is relevant to the proposed array n.1, and the red line indicates, as usual, the edge of the one-look azimuth region for burst 1 at the nearest range. To be compared with the IS curves reported in Fig. 6.

According to this analysis, we can safely conclude that, as expected, the IS curve is an effective figure of merit to measure the array performance in terms of scalloping control.

REFERENCES

[1] M. Zimmermanns and C. Roemer, "Copernicus HPCM: ROSE-L SAR instrument and performance overview," in *Proc. 14th Eur. Conf. Synth. Aperture Radar*, Leipzig, Germany, Jul. 2022, pp. 1–6.

[2] M. W. J. Davidson and R. Furnell, "ROSE-L: Copernicus L-band SAR mission," in *Proc. IEEE Int. Geosci. Remote Sens. Symp. IGARSS*, Brussels, Belgium, Jul. 2021, pp. 872–873.

[3] A. Moreira, P. Prats-Iraola, M. Younis, G. Krieger, I. Hajnsek, and K. P. Papathanassiou, "A tutorial on synthetic aperture radar," *IEEE Geosci. Remote Sens. Mag.*, vol. 1, no. 1, pp. 6–43, Mar. 2013.

[4] K. Tomiyasu, "Conceptual performance of a satellite borne, wide swath synthetic aperture radar," *IEEE Trans. Geosci. Remote Sens.*, vol. GE-19, no. 2, pp. 108–116, Apr. 1981.

[5] J. H. Blythe, "Radar systems," U.S. Patent 4 253 098, Feb. 24, 1981.

[6] N. Gebert, G. Krieger, and A. Moreira, "Digital beamforming on receive: Techniques and optimization strategies for high-resolution wide-swath SAR imaging," *IEEE Trans. Aerosp. Electron. Syst.*, vol. 45, no. 2, pp. 564–592, Apr. 2009.

[7] A. Currie and M. A. Brown, "Wide-swath SAR," *IEE Proc. F Radar Signal Process.*, vol. 139, no. 2, pp. 122–135, Apr. 1992.

[8] G. Krieger, N. Gebert, and A. Moreira, "Unambiguous SAR signal reconstruction from nonuniform displaced phase center sampling," *IEEE Geosci. Remote Sens. Lett.*, vol. 1, no. 4, pp. 260–264, Oct. 2004.

[9] C. Balanis, *Antenna Theory: Analysis and Design*. New York, NY, USA: Harper & Row, 1982.

[10] S. Perna, F. Longo, S. Zoffoli, M. Davidson, L. Lannini, and R. Lanari, "Advanced ScanSAR capabilities enabled by optimized antenna array azimuth radiation patterns: The ROSE-L case study," in *Proc. IEEE Int. Geosci. Remote Sens. Symp.*, Kuala Lumpur, Malaysia, Jul. 2022, pp. 7401–7404.

[11] D. Tomsu, S. Trumpf, and P. Prats-Iraola, "Exploitation of 2-look ScanSAR with ROSE-L for along-track surface deformation measurements," in *Proc. ESA Workshop*, Leeds, U.K., 2023. [Online]. Available: https://fringe2023.esa.int/iframe-agenda/files/presentation-401.pdf

[12] G. Franceschetti and R. Lanari, *Synthetic Aperture Radar Processing*. New York, NY, USA: CRC Press, 1999.

[13] U.S. Geological Survey. (Oct. 2015). *The Shuttle Radar Topography Mission (SRTM) Collection User Guide*. [Online]. Available: https://lpdaac.usgs.gov/documents/179/SRTM_User_Guide_V3.pdf

[14] A. Pepe, A. Bertran Ortiz, P. R. Lundgren, P. A. Rosen, and R. Lanari, "The Stripmap–ScanSAR SBAS approach to fill gaps in stripmap deformation time series with ScanSAR data," *IEEE Trans. Geosci. Remote Sens.*, vol. 49, no. 12, pp. 4788–4804, Dec. 2011.

[15] Y. Qin, D. Perissin, and J. Bai, "A common 'stripmap-like' interferometric processing chain for TOPS and ScanSAR wide swath mode," *Remote Sens.*, vol. 10, p. 1504, Sep. 2018.

[16] N. Yague-Martinez, P. Prats-Iraola, S. Wollstadt, and A. Moreira, "The 2-look TOPS mode: Design and demonstration with TerraSAR-X," *IEEE Trans. Geosci. Remote Sens.*, vol. 57, no. 10, pp. 7682–7703, Oct. 2019.

[17] P. Prats-Iraola, N. Yague-Martinez, S. Wollstadt, T. Kraus, and R. Scheiber, "Demonstration of the applicability of 2-look burst modes in non-stationary scenarios with TerraSAR-X," in *Proc. 11th Eur. Conf. Synth. Aperture Radar*, Hamburg, Germany, Jun. 2016, pp. 1–6.

[18] F. De Zan and A. M. Guarnieri, "TOPSAR: Terrain observation by progressive scans," *IEEE Trans. Geosci. Remote Sens.*, vol. 44, no. 9, pp. 2352–2360, Sep. 2006.

[19] R. Bamler and M. Eineder, "ScanSAR processing using standard high precision SAR algorithms," *IEEE Trans. Geosci. Remote Sens.*, vol. 34, no. 1, pp. 212–218, Jan. 1996.

[20] R. Bamler, "Optimum look weighting for burst-mode and ScanSAR processing," *IEEE Trans. Geosci. Remote Sens.*, vol. 33, no. 3, pp. 722–725, May 1995.

[21] R. Grandin, E. Klein, M. Métois, and C. Vigny, "Three-dimensional displacement field of the 2015 M_w8.3 Illapel earthquake (Chile) from across- and along-track Sentinel-1 TOPS interferometry," *Geophys. Res. Lett.*, vol. 43, no. 6, pp. 2552–2561, Mar. 2016.

[22] R. Torres et al., "GMES Sentinel-1 mission," *Remote Sens. Environ.*, vol. 120, pp. 9–24, May 2012.

[23] O. M. Bucci and S. Perna, "A deterministic two dimensional density taper approach for fast design of uniform amplitude pencil beams arrays," *IEEE Trans. Antennas Propag.*, vol. 59, no. 8, pp. 2852–2861, Aug. 2011.

[24] J. C. Curlander and R. N. McDonough, *Synthetic Aperture Radar: Systems & Signal Processing*. Hoboken, NJ, USA: Wiley, 1991.

[25] M. Shimada, "A new method for correcting ScanSAR scalloping using forests and inter-SCAN banding employing dynamic filtering," *IEEE Trans. Geosci. Remote Sens.*, vol. 47, no. 12, pp. 3933–3942, Dec. 2009.

[26] S. Wollstadt, P. Prats, M. Bachmann, J. Mittermayer, and R. Scheiber, "Scalloping correction in TOPS imaging mode SAR data," *IEEE Geosci. Remote Sens. Lett.*, vol. 9, no. 4, pp. 614–618, Jul. 2012.

[27] M. Manzo et al., "Surface deformation analysis in the ischia island (Italy) based on spaceborne radar interferometry," *J. Volcanol. Geothermal Res.*, vol. 151, no. 4, pp. 399–416, Mar. 2006.

Stefano Perna (Senior Member, IEEE) received the Laurea degree (summa cum laude) in telecommunication engineering and the Ph.D. degree in electronic and telecommunication engineering from the Università degli Studi di Napoli "Federico II," Naples, Italy, in 2001 and 2006, respectively.

In 2003, 2005, and 2006, he received grants from the Italian National Research Council (CNR), Naples, to be spent at the Istituto per il Rilevamento Elettromagnetico dell'Ambiente (IREA), Naples, for research in the field of remote sensing. Since 2006, he has been with the Dipartimento di Ingegneria (DI), Università degli Studi di Napoli "Parthenope," Naples, where he is currently a Professor of electromagnetic fields. He also holds the position of Adjunct Researcher at IREA-CNR. Since 2015, he has been collaborating with the Argentinian National Council of Technical and Scientific Research (CONICET) on activities relevant to the focusing and processing of airborne and spaceborne synthetic aperture radar (SAR) data. In 2016, he was a Visiting Professor with the Departamento de Teoría de la Señal y Comunicaciones, Universitat Politècnica de Catalunya (UPC), Barcelona, Spain. He is responsible for several research projects relevant to the realization and testing of novel radar systems, and the focusing and processing of airborne SAR data. Since 2020, he has been a member of the Mission Advisory Group (MAG) of the PLATINO-1 SAR mission funded by the Italian Space Agency (ASI). His main research interests are in the field of microwave remote sensing and electromagnetics: airborne SAR data modeling and processing, airborne SAR interferometry, modeling of electromagnetic scattering from natural surfaces, synthesis of antenna arrays, antenna characterization, and measurement in anechoic and reverberating chambers.

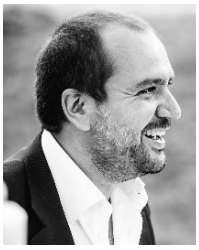

Francesco Longo was born in Italy in 1971. He received the M.Sc. degree in aerospace engineering from the "Politecnico di Torino," Turin, Italy, in 1997, the M.Sc. degree in astronautical engineering from the University of Rome "Sapienza," Rome, Italy, in 2000, the Ph.D. degree in aerospace engineering from the University of Rome "Sapienza," in 2003, and the master's degree in space systems engineering (MSSE) from the Delft University of Technology (NL), Delft, The Netherlands, in 2010.

He is currently the Head of the Earth Observation and Operations Division, Italian Space Agency, Rome.

Dr. Longo is a National Delegate of the ESA Earth Observation Program Board (PBEO) and an Expert of the EU Copernicus Committee.

Simona Zoffoli received the degree in physics from Università La Sapienza, Rome, Italy, in 1997, and the Ph.D. degree in geodesy and geomatics from the Politecnico di Milano, Milan, Italy, in 2009.

In 1998, she joined the Italian Space Agency (ASI), Rome, working in Earth observation programs. As a Program Manager, she has managed several science and application initiatives mainly focused on the use of Earth observation data to support disaster risk management activities and environmental monitoring. During her career, she has also been involved in the formulation studies of Earth observation missions and payloads. She was the ASI Program Manager for the LIMADOU—CSES-01 mission launched in 2018 and is currently the ASI Program Manager for the LIMADOU—CSES-02 mission and the SBG-TIR mission. Since 2011, she has been a Delegate of the ESA DOSTAG, and she is currently the Head of Earth Science Office under the ASI Earth Observation Unit.

Dr. Zoffoli was the Vice Chair (2015 to 2017) and than the Chair (2017 to 2019) of the CEOS WG Disasters.

Malcolm Davidson was born in Canberra, ACT, Australia, in 1968. He received the B.Sc. degree (Hons.) in physics from the University of Toronto, Toronto, ON, Canada, in 1990, the M.Sc. degree in image processing and remote sensing from The University of Edinburgh, Edinburgh, U.K., in 1992, and the Ph.D. degree in physics from the Rheinische Friedrich-Wilhelms-Universität Bonn, Bonn, Germany, in 1997.

From 1997 to 2001, he worked as a Research Associate with the Centre D'Etudes de la Biosphere (CESBIO), Toulouse, France. Since 2001, he has been a Staff Member of the Earth and Mission Science Division, European Space Research and Technology Centre (ESTEC), European Space Agency (ESA), Noordwijk, The Netherlands. At ESA, he holds the role of Mission Scientist for the Copernicus SENTINEL-1 and ROSE-L missions. His main responsibilities concern the formulation of mission requirements for this mission and chairing mission advisory groups. He was also appointed as the Head of the Campaigns Section in 2009 and is responsible for managing the scientific campaign activity program, which includes ground, tower, and airborne campaigns in support of Earth observation (EO) missions and mission science.

Lorenzo Iannini received the master's degree in telecommunications engineering and the Ph.D. degree from the Politecnico di Milano, Milan, Italy, in 2008 and 2013, respectively. His Ph.D. dissertation was on the polarimetric calibration of synthetic aperture radar (SAR).

He continued his research with the Geoscience and Remote Sensing Department, Delft University of Technology, Delft, The Netherlands, until 2020. He is currently providing science support to the future Copernicus SAR missions with the European Space Research and Technology Centre (ESTEC), European Space Agency, Noordwijk, The Netherlands. Throughout his career, he engaged in multiple project initiatives aimed at devising radar processing algorithms for land applications, designing SAR system concepts, and evaluating spaceborne SAR system performance.

Riccardo Lanari (Fellow, IEEE) received the Laurea degree in electronic engineering (summa cum laude) from the University of Napoli "Federico II," Naples, Italy, in 1989.

In 1989, he joined IRECE and then IREA, Italian Council of Research (CNR), Naples. He was a Visiting Scientist with different foreign research institutes, including the German Aerospace Research Establishment (DLR), Oberpfaffenhofen, Germany, in 1991 and 1994, the Institute of Space and Astronautical Science (ISAS), Sagamihara, Japan, in 1993, and the Jet Propulsion Laboratory (JPL), Pasadena, CA, USA, in 1997, 2004, and 2008. He was an Adjunct Professor with the University of Sannio, Benevento, Italy, from 2000 to 2003, and a main Lecturer with the Institute of Geomatics, Barcelona, Spain, from 2000 to 2008. From December 2010 to September 2021, he was the Director of IREA, where he currently holds the position of Research Director. Moreover, he has achieved the national scientific habilitation as a Full Professor of telecommunications in December 2013 and a Full Professor of geophysics in February 2014. He has more than 30 years of research experience in the remote sensing field, particularly on spaceborne and airborne synthetic aperture radar (SAR) and SAR interferometry (InSAR) data processing method developments, and their applications in geosciences. On these topics, he holds two patents, and he has coauthored the book *Synthetic Aperture Radar Processing* (CRC Press, 1999) and more than 500 scientific publications (150 in ISI journals) that have, nowadays, more than 18 000 citations (H-index = 65, source: Google Scholar).

Mr. Lanari received a recognition from NASA in 1999, a group award in 2001 for his activities related to the SRTM mission, the Dorso Prize in 2015, for the Special Section "Research," held under the patronage of the Senate of the Italian Republic, the Christiaan Huygens Medal of the European Geosciences Union (EGU) in 2017, and the Fawwaz Ulaby Distinguished Achievement Award of the IEEE Geoscience and Remote Sensing Society (GRSS) in 2020. He was awarded the title of Knight of the Order of Merit of the Italian Republic (Cavaliere dell'Ordine al Merito della Repubblica Italiana) by the President of the Italian Republic, in 2023. He was a member of the National Commission for the Prevision and Prevention of Big Risks (Commissione Nazionale Grandi Rischi), from 2017 to 2023. Since 2022, he has been an Expert of the Italian Delegation of the Copernicus Program (for the Spatial Program Committee). He has been a member of the Advisory Groups of the Sentinel-1 Next Generation mission since 2020, the ROSE-L mission since 2020, and the COSMO-SkyMed missions of the first and second generation, from 2015 to 2019 and since 2021. Since 2001, he has been a Distinguished Speaker of the GRSS of the IEEE. He has lectured in several national and foreign universities and research centers, and served as a chairperson/convener and/or scientific program committee member for many international conferences.

Open Access funding provided by 'Consiglio Nazionale delle Ricerche-CARI-CARE-ITALY'
within the CRUI CARE Agreement